Research Square

Preprints are preliminary reports that have not undergone peer review.
They should not be considered conclusive, used to inform clinical practice,
or referenced by the media as validated information.

Post-engagement CAR release, rather than equilibrium affinity, governs repetitive stromal targeting by CAR-NK cells

Mihue Jang

mihue@kist.re.kr

Korea Institute of Science and technology https://orcid.org/0000-0002-2135-2983

Seung hun Shin

Korea Institute of Science and Technology

Jisu Hong

Seoul National University College of Medicine

Daeun Kim

Seoul National University

Su-Min Yee

Korea Institute of Science and Technology

Hye Won Lim

Seoul National University College of Medicine

Jaejun Han

Seoul National University College of Medicine

Hoibin Jeong

Korea Basic Science Institute

Seung-Hae Kwon

Jong Hyeon Yoon

Korea University

Yujin Jin

Seoul National University College of Medicine

Hyun Jung Kim

University of Ulsan College of Medicine

Sangwon Yoon

UCI therapeutics

Daechan Park

Department of Molecular Science and Technology, Advanced College of Bio-Convergence Engineering, Ajou University, Suwon, South Korea https://orcid.org/0000-0003-4991-5247

Song Cheol Kim

University of Ulsan College of Medicine https://orcid.org/0000-0003-4552-4169

Chang Han Lee

Seoul National University College of Medicine https://orcid.org/0000-0002-7156-4423

Article

Keywords:

Posted Date: October 13th, 2026

DOI: https://doi.org/10.21203/rs.3.rs-11261510/v1

License: This work is licensed under a Creative Commons Attribution 4.0 International License. Read Full License

Additional Declarations: Yes there is potential Competing Interest. S.H.S., J.H.Y., J.S.H., C-H.L. and M.J are listed as inventors on a patent (KR 10-2023-0064534). The authors declare no other competing interests.

Post-engagement CAR release, rather than equilibrium affinity, governs repetitive stromal targeting by CAR-NK cells

Seung Hun Shin[1,2,†], Jisu Hong[3,4,15,†], Daeun Kim[5,6,7], Su-Min Yee[1], Hye Won Lim[3,4], Jaejun Han[4], Hoibin Jeong[8], Seung Hae Kwon[8], Jong Hyeon Yoon[9], Yujin Jin[3,4], Hyun Jung Kim[11], Sangwon Yoon[12], Daechan Park[6,13], Song Cheol Kim[14]*, Chang-Han Lee[3,4,10,15]*, Mihue Jang[1,16,17]*

[1]Medicinal Materials Research Center, Biomedical Research Division, Korea Institute of Science and Technology, Seoul, 02792, Republic of Korea

[2]Department of Biotechnology, College of Life Sciences and Biotechnology, Korea University, Seoul, 02841, Republic of Korea

[3]Department of Biomedical Sciences, Seoul National University College of Medicine, Seoul, 03080, Republic of Korea

[4]Department of Pharmacology, Seoul National University College of Medicine, Seoul, 03080, Republic of Korea

[5]Institute of Chemical Processes, Seoul National University, Seoul, 08826, Republic of Korea

[6]Department of Molecular Science and Technology, Ajou University, Suwon, 16499, Republic of Korea

[7]Ajou Energy Science Research Center, Ajou University, Suwon, 16499, Republic of Korea

[8]Metropolitan Seoul Center, Korea Basic Science Institute, Seoul, 02841, Republic of Korea

[9]School of Biosystems and Biomedical Sciences, College of Health Science, Korea University, Seoul, 02841, Republic of Korea

[10]Cancer Research Institute, Seoul National University College of Medicine, Seoul, 03080, Republic of Korea

[11]Department of Medicine, University of Ulsan College of Medicine, Seoul, 05505, Republic of Korea

[12]Corporate Research & Development Center, UCI Therapeutics, Guri, 11901, Republic of Korea

[13]College of Advanced Bio-Convergence Engineering, Ajou University, Suwon, 16499, Republic of Korea

[14]Division of Hepato-Biliary and Pancreatic Surgery, Department of Surgery, University of Ulsan College of Medicine, BK 21 project, Asan Medical Center, Seoul, 05505, Republic of Korea

[15]BK21 FOUR Biomedical Science Project, Seoul National University College of Medicine, Seoul, 03080, Republic of Korea

[16]KHU-KIST Department of Converging Science and Technology, Kyung Hee University, Seoul, 02447, Republic of Korea

[17]Division of Bio-Medical Science and Technology, KIST School, University of Science and Technology (UST), Seoul, 02792, Republic of Korea

[†]These authors contributed equally to this work

*Corresponding authors

Mihue Jang, Ph.D. Tel: +82-2-958-6618; fax: +82-2-958-5909; email: mihue@kist.re.kr

Chang-Han Lee, Ph.D. Tel: +82-2-740-8278; email: chlee-antibody@snu.ac.kr

Song Cheol Kim, M.D., Ph.D. Email: drksc@amc.seoul.kr

Abstract

Chimeric antigen receptor (CAR) cell therapies have transformed haematological cancer treatment but remain largely ineffective against desmoplastic solid tumours, where a fibroblast-rich matrix restricts effector cell infiltration. Depleting that stroma requires repeated clearance of abundant fibroblasts, yet CAR binders are still commonly selected and optimized around equilibrium affinity. Here we show that how quickly a CAR releases antigen after killing, rather than how tightly it binds, governs repetitive stromal targeting. We identified endoglin (CD105) on the abundant fibroblasts organizing this barrier in pancreatic cancer, then screened CD105 binders in matched CARs. The lead binder bound 40-fold more weakly than the reference antibody yet killed fibroblasts far more effectively, dissociating 11-fold faster. The difference lay after cytolysis: killing was equally fast, release was not, and faster release reset the synapse, reduced antigen trogocytosis and sustained serial killing. In fibroblast-rich tumours, a humanized variant opened a window for mesothelin-directed CAR-T and CAR-NK cells. Release kinetics therefore determine whether a CAR cell works as a reusable stromal-remodelling effector, and tuning them may improve any CAR that must clear abundant targets.

Introduction

Chimeric antigen receptor (CAR)-based cell therapies, including CAR-T and CAR-natural killer (NK) cells, have transformed the treatment of haematological malignancies[1, 2], but their activity in solid tumours remains constrained by physical, cellular and biochemical barriers

within the tumour microenvironment[3, 4]. This limitation is particularly pronounced in pancreatic ductal adenocarcinoma (PDAC), where desmoplasia, fibroblast expansion and dense extracellular matrix (ECM) deposition restrict immune-cell infiltration and impair effector function[5-7]. Cancer-associated fibroblasts (CAFs) form matrix-rich barriers, recruit immunosuppressive populations and release mediators such as transforming growth factor-β (TGF-β) and interleukin (IL)-6 that attenuate NK-cell activity[8-15]. These observations position disease-associated CAFs as actionable stromal targets, motivating a stroma-first architecture in which the microenvironment is remodelled before a tumour-directed product is deployed.

CD105/endoglin (*ENG*) is an attractive stromal target because it is an accessory co-receptor for TGF-β superfamily members[16] and is expressed in CAF subsets across solid tumours[17-19]. In pancreatic cancer, $CD105^+$ fibroblasts have been linked to TGF-β responsiveness, stromal remodelling and immunomodulatory phenotypes[20]. Although CD105 is also expressed in endothelial compartments[21], fibroblast-resolved analyses can distinguish $CD105^+$ CAF states from vascular expression. Conventional CD105 antibody blockade, including carotuximab (TRC105), was well tolerated but did not provide substantial efficacy in later-stage trials[22-25], suggesting that passive blockade is insufficient to dismantle a fibroblast-rich barrier and motivating cellular modalities capable of actively eliminating tumour-supportive $CD105^+$ CAFs.

Clearing a fibroblast barrier requires each effector to be reused. CAR activity is shaped not only by specificity and equilibrium affinity but also by cell-level avidity, antigen density, receptor internalization, trogocytosis, CAR degradation and CAR–antigen disengagement kinetics[26-29]. Maximal equilibrium affinity does not necessarily confer optimal cellular activity when sustained serial engagement is required. This is especially relevant to CAF targeting,

where stromal remodelling may depend on eliminating many fibroblasts rather than adhering durably to individual cells. We therefore reasoned that CD105-specific scFvs should be selected by integrated functional and kinetic profiling, and hypothesized that a binder supporting sufficient engagement followed by rapid post-killing release would preserve CAR availability and enable repetitive stromal-cell elimination.

Here we establish CD105^{+} CAFs as functional organizers of a TGF-β-associated, fibronectin-rich and immune-restrictive stromal niche in PDAC. Using plasma B-cell screening coupled with functional and kinetic CAR-NK profiling, we identify CLEN24 as a faster-off CD105 binder. When incorporated into a CAR (EN24), CLEN24 retained sufficient cellular avidity for cytolysis, induced the least trogocytosis among the constructs tested and enabled the fastest immune-synapse reset after killing. Humanization retained this phenotype in primary NK cells, and we incorporate hEN24-CD105-CAR-NK cells into a two-wave strategy in which stromal priming precedes mesothelin (MSLN)-directed CAR-NK or CAR-T therapy.

Results

CD105 marks and sustains an abundant, matrix-organizing fibroblast state in pancreatic cancer

We first asked whether CD105, encoded by *ENG*, is merely a marker of pancreatic fibroblasts or actively contributes to CAF-mediated tumour-promoting activity. Surface CD105 was low or undetectable in NK cells and most pancreatic cancer lines, but was readily detected in CD105-transduced controls (**Extended Data Fig. 1a**). In patient-derived CAFs, it was prominently expressed by both flow cytometry and immunoblotting (**Fig. 1a and Extended**

Data Fig. 1b,c). CD105 immunohistochemistry showed stromal-enriched staining in human PDAC tissues that was low or undetectable in non-neoplastic pancreas under the same conditions (**Fig. 1b**). CD105 is therefore a fibroblast-enriched surface antigen in pancreatic cancer, and its limited expression on NK cells may reduce the potential for CAR-NK fratricide.

Treatment of human primary pancreatic fibroblasts (HPPFs) with TGF-β1 increased CD105 together with α-SMA by immunoblotting (**Fig. 1c**), and immunofluorescence confirmed induction of CD105 protein (**Fig. 1d**). TGF-β1 is therefore sufficient to induce CD105 as part of an activated fibroblast phenotype. To test whether fibroblast-intrinsic CD105 contributes functionally, we generated *ENG*-knockout (KO) fibroblasts, hereafter CD105-deficient fibroblasts, from HPPFs and patient-derived CAFs and validated them by flow cytometry (**Extended Data Fig. 1d**). Relative to Cas9-only control fibroblasts, CD105-deficient fibroblasts showed impaired motility (**Fig. 1e, Supplementary Fig. 1 and Supplementary Videos 1–4**). They also supported less cancer-cell invasion through Matrigel (**Fig. 1f**) and less transendothelial migration across a human umbilical vein endothelial cell (HUVEC) monolayer (**Fig. 1g**). Conditioned media from CD105-deficient fibroblasts also maintained higher E-cadherin in AsPC-1 and PANC-1 cells, consistent with reduced paracrine drive towards an epithelial-to-mesenchymal transition (EMT)-like phenotype (**Supplementary Fig. 2**).

CD105 is therefore not simply a marker of activated fibroblasts but is functionally required for their pro-invasive behaviour. We next asked whether $CD105^{+}$ CAFs also limit intratumoural NK-cell accumulation *in vivo*.

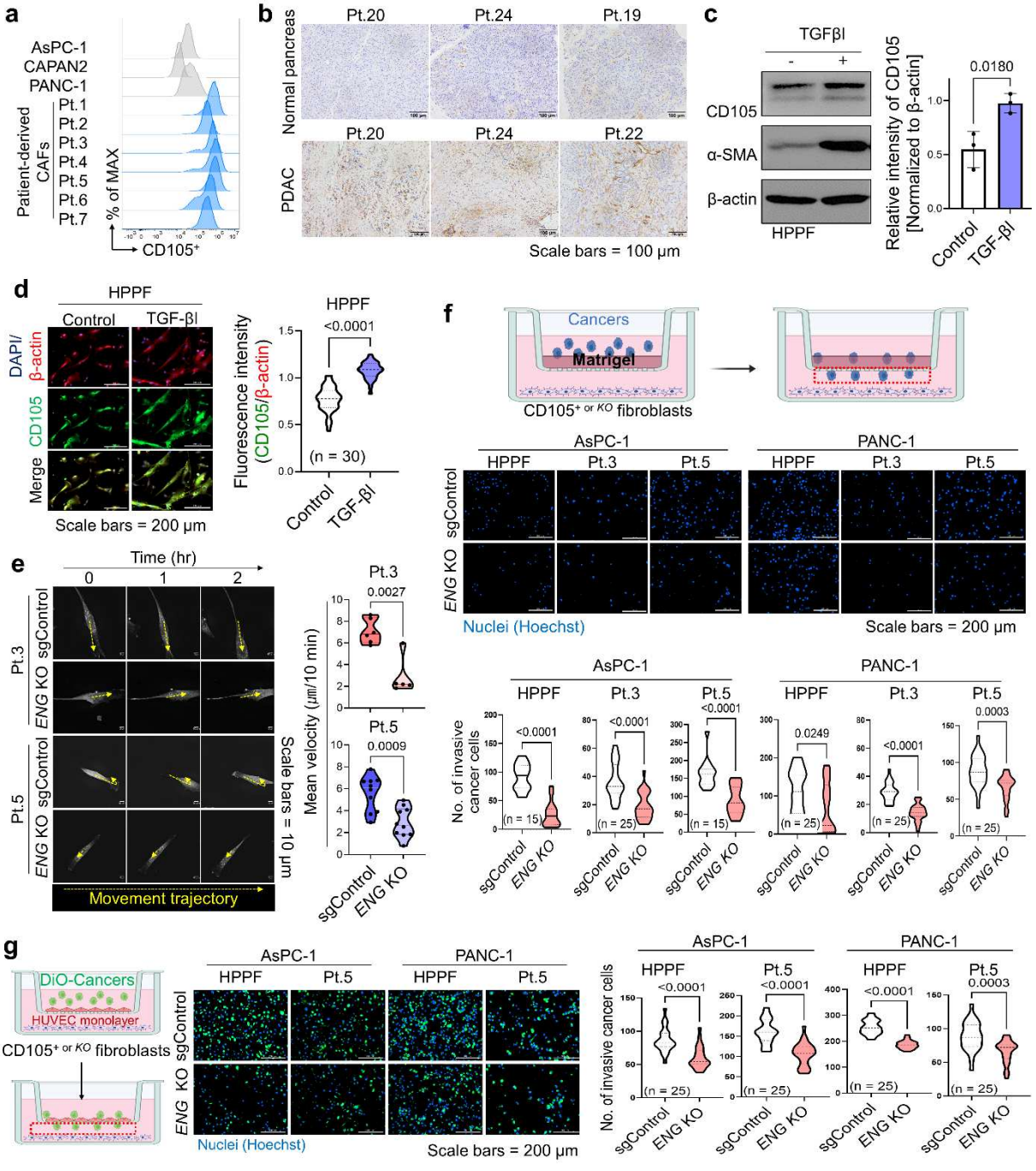


Fig. 1. TGF-β-induced CD105 expression defines a pro-invasive pancreatic fibroblast state that promotes tumour-cell invasion and transendothelial migration. a, Flow cytometry of surface ENG/CD105 across pancreatic cancer cell lines (grey) and patient-derived CAFs (blue). **b,** Representative immunohistochemical staining of CD105 in non-neoplastic pancreas (Pt.20, Pt.24, Pt.19) and PDAC tissue (Pt.20, Pt.24, Pt.22). Scale bars, 100 µm. **c,**

Immunoblot of CD105 and α-SMA in HPPFs treated with or without TGF-β1 (10 ng ml^{-1}, 48 h). Right, quantification of CD105 normalized to β-actin (n = 3 independent experiments). **d,** Representative immunofluorescence of CD105 in HPPFs treated with or without TGF-β1 (10 ng ml^{-1}, 48 h). Nuclei, β-actin and CD105 are shown in blue, red and green, respectively. Right, quantification of CD105 intensity normalized to β-actin intensity. Data are presented as the mean ± s.d. from two independent experiments, with 15 foci analysed per experiment. Scale bars, 200 μm. **e,** Time-lapse tracking of Cas9-only control and *ENG*-knockout (KO) CAF motility. Representative trajectories (left) and mean velocity (right) (n = 5 for Pt.3 and n = 10 for Pt.5 at the single-cell resolution). Scale bars, 10 μm. **f,** Matrigel invasion assay of pancreatic cancer cells co-cultured with control or *ENG*-KO fibroblasts. Representative images and quantification of $Hoechst^+$ invasive cells for AsPC-1 and PANC-1 (n = 15 or 25 fields). Scale bars, 200 μm. **g,** HUVEC monolayer transmigration assay of DiO-labelled cancer cells in the presence of control or *ENG*-KO fibroblasts. Representative images and quantification of transmigrated cells (n = 25 fields). Scale bars, 200 μm. Pt., patient-derived CAF donor. Each point in the violin plots represents an individual imaged field or cell, as indicated. Data are mean ± s.d. P values were calculated using unpaired two-tailed t-tests.

$CD105^+$ CAFs are abundant organizers of an NK-excluding ECM niche associated with adverse disease

We next asked whether $CD105^+$ fibroblasts shape tumour progression, matrix organization and immune access *in vivo*. *ENG* KO reduced ECM- and mesenchymal-associated transcripts (*FN1*, *VIM*, *COL1A1*) in HPPFs and two independent patient-derived CAFs (**Fig. 2a**), with

corresponding reductions in fibronectin, vimentin and collagen alpha-1(I) chain protein (**Fig. 2b**). Co-implantation of HPPFs increased PANC-1 tumour radiant efficiency relative to PANC-1 cells alone (**Extended Data Fig. 2**). We then co-implanted AsPC-1 cells with Cas9-only control or *ENG*-KO patient-derived CAFs into NOD–scid IL2Rγ-null (NSG) mice (**Fig. 2c**). Control CAFs accelerated tumour growth relative to AsPC-1 alone, whereas *ENG*-KO CAFs lost this activity. Haematoxylin and eosin staining of representative lung sections showed more extensive pulmonary lesions in control CAF-containing tumours (**Fig. 2d**), and immunofluorescence showed reduced fibronectin in *ENG*-KO CAF-containing xenografts (**Fig. 2e**).

To ask whether $CD105^+$ CAFs limit intratumoural NK-cell accumulation, we adoptively transferred DiD-labelled primary NK cells and quantified intratumoural human $CD45^+DiD^+$ cells (**Fig. 2f and Supplementary Fig. 3**). *ENG*-KO CAF-containing tumours showed greater NK-cell accumulation than control CAF-containing tumours even after normalization to tumour weight, indicating that recovery was not explained solely by tumour burden and supporting a direct role for $CD105^+$ CAFs in limiting intratumoural NK-cell accumulation.

We then examined clinical relevance. High *ENG* expression within basal-like tumour spots was associated with poorer overall survival (**Fig. 2g**). To define the fibroblast state itself, we analysed public single-cell RNA-sequencing data from treatment-naïve (n = 20; 159,415 cells) and treated (n = 7; 71,893 cells) PDAC tumours[30]. Uniform manifold approximation and projection (UMAP) resolved the major compartments in both cohorts, and fibroblasts were identified by selective enrichment of *COL3A1*, *COL1A2*, *COL1A1*, *SFRP2* and *DCN* (**Extended Data Fig. 3**). Because *ENG* was also detected in endothelial cells, we restricted all ENG^+ versus ENG^- comparisons to the fibroblast compartment.

182 *ENG*$^{+}$ fibroblasts were enriched for EMT, TGF-β signalling and stromal remodelling hallmark
183 programmes in both cohorts (**Extended Data Fig. 4a,b**). Because the analysis was restricted
184 to fibroblasts, EMT enrichment reflects mesenchymal activation rather than epithelial lineage
185 transition. Gene set enrichment analysis (GSEA) confirmed enrichment of hallmark TGF-β
186 signalling and of ECM assembly and organization in *ENG*$^{+}$ fibroblasts across both cohorts (**Fig.**
187 **2h**), with concordant upregulation of ECM-associated genes (**Extended Data Fig. 4c**). To
188 assess the robustness of the cell-level GSEA while accounting for inter-donor variability and
189 potential pseudoreplication, GSEA was additionally performed using a donor-level pseudobulk
190 approach. The direction of enrichment was generally preserved, although NES values were
191 attenuated and FDR-adjusted significance was reduced for some gene sets (**Supplementary**
192 **Fig. 4**). Spatially, Visium profiles from 36 tumour cores showed that *ENG*$^{+}$ CAF-enriched
193 regions co-localized with ECM and myofibroblastic CAF-like signatures rather than with
194 tumour-cell signatures (**Extended Data Fig. 4d**). They also overlapped antigen-presenting
195 CAF-like and T-cell signatures, marking stromal interfaces where matrix organization and
196 immune-cell positioning converge. Ligand–receptor analysis showed enrichment of TGF-
197 β/CD105-axis and ECM–integrin interactions in the same regions (**Extended Data Fig. 4e**).
198 Together, these data identify CD105^{+} CAFs as abundant organizers of an NK-excluding ECM
199 niche in clinically adverse disease and provide a rationale for targeting them as stromal-priming
200 effectors.

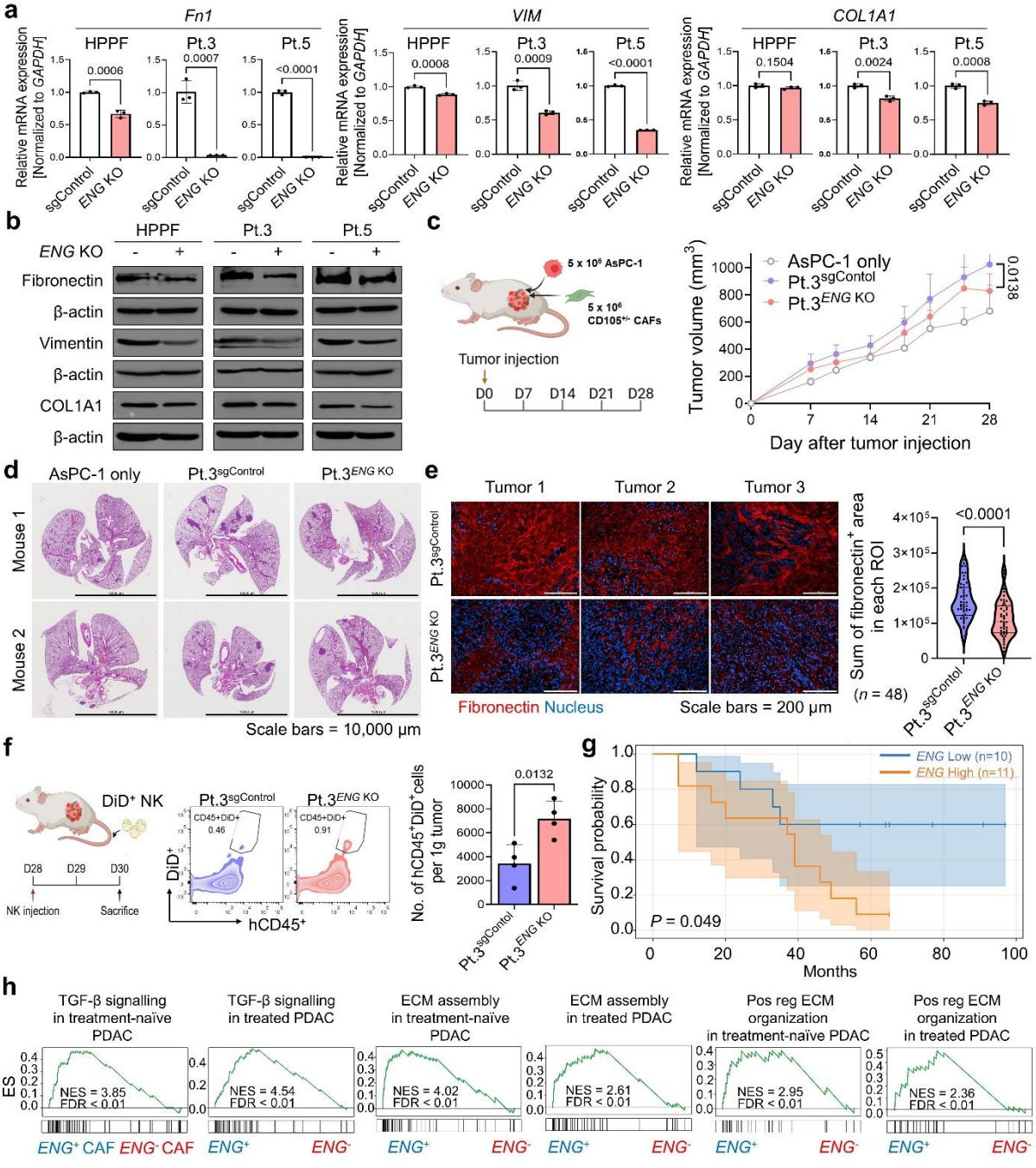


Fig. 2. CD105⁺ CAFs remodel the ECM and limit intratumoural NK cell accumulation in clinically adverse disease. a, Quantitative PCR of *FN1*, *VIM* and *COL1A1* in Cas9-only control and *ENG*-KO HPPFs and patient-derived CAFs, normalized to *GAPDH* (n = 3 independent experiments). **b,** Immunoblot of matrix- and mesenchymal-associated proteins in

the same cells. β-actin was the loading control. **c,** Schematic of the subcutaneous co-implantation xenograft model and tumour growth curves. AsPC-1 cells were implanted alone or with control or *ENG*-KO patient-derived CAFs into NSG mice (n = 7 mice per group). **d,** Representative haematoxylin and eosin-stained lung sections from the indicated groups (two mice shown per group). Scale bars, 10,000 μm. **e,** Immunofluorescence of fibronectin in tumour tissue from the indicated groups. Fibronectin and nuclei are shown in red and blue, respectively. Each point represents an analysed region of interest from Pt.3 xenografts (16 regions analysed per tumour from three tumours per group). Scale bars, 200 μm. **f,** Schematic and quantification of DiD-labelled primary NK-cell adoptive transfer into mice bearing control or *ENG*-KO CAF-containing xenografts (n = 4 mice per group). Cell numbers were normalized to tumour weight. Panels **c**–**f** are from a single experiment: of the seven tumours per group in **c**, four were dissociated for flow cytometry (**f**) and three were processed for tissue staining (**e**). **g,** Kaplan–Meier analysis of overall survival according to patient-level *ENG* expression within the indicated ROI. Patients were stratified into *ENG*-high (n = 11) and *ENG*-low (n = 10) groups using the median patient-level *ENG* expression as the cut-off. P value was determined by a two-sided log-rank test. Hazard ratio (HR) and 95% confidence interval (CI) were estimated using a univariable Cox proportional hazards model. **h,** GSEA showing enrichment of hallmark TGF-β signalling (hallmark collection H) and of ECM assembly and positive regulation of ECM organization (GO:BP collection C5) in ENG^{+} versus ENG^{-} fibroblasts from treatment-naïve and treated PDAC samples. Normalized enrichment scores (NES) and false-discovery rates (FDR) are shown. Data are mean ± s.d. unless otherwise indicated. P values were calculated using unpaired two-tailed t-tests for two-group comparisons and two-way analysis of variance (ANOVA) followed by Tukey's multiple comparisons test for tumour growth curves.

Function-first screening identifies EN24 as the most productive CD105-CAR binder despite unremarkable binding potency

To target CD105$^+$ CAFs actively, we established a plasma B-cell discovery workflow. Mice were immunized with the recombinant CD105 ectodomain, and CD138$^+$ plasma cells were screened on a Beacon optofluidic platform in three parallel assays (**Fig. 3a and Extended Data Fig. 5**). Antibody sequences from CD105-reactive events were cloned, grouped into clonal clusters and prioritized for recombinant scFv validation (**Extended Data Figs. 6 and 7**). Antibody clones are designated CLEN01–CLEN25 and their CAR counterparts EN*nn*.

We advanced one representative from each clonal cluster, sampling distinct clonal families and Beacon profiles rather than selecting for binding strength, alongside the reference CD105 antibodies TRC105 and 9H10 (**Fig. 3b**). Sequences falling in a cluster that was already represented were therefore not carried forward, however strongly they bound. ELISA and flow cytometry identified six scFvs (CLEN06, CLEN07, CLEN11, CLEN12, CLEN21 and CLEN24) that bound both recombinant and native cell-surface CD105, with minimal binding to CD105$^-$ cells (**Fig. 3c,d, Supplementary Figs. 5 and 6 and Supplementary Tables 1 and 2**). Competitive epitope binning separated the prioritized binders into discrete groups (**Fig. 3e**) that mapped to spatially distinct regions of the CD105 ectodomain (**Fig. 3f**), yielding a sequence-, family- and epitope-diverse panel for matched CAR evaluation.

Selected scFvs were then built into matched second-generation CD105-CAR-NK-92 constructs and screened against endogenous CD105$^+$ CAF targets by real-time caspase-3/7 imaging (**Fig.**

3g). Despite shared specificity, constructs differed markedly in CAF killing (**Fig. 3h,i**), and quantification at 3 h and 6 h identified EN24-CAR-NK-92 cells as producing the strongest and most sustained induction of CAF apoptosis (**Fig. 3j**). EN24-CAR-NK-92 cells also showed antigen-dependent cytotoxicity, degranulation and interferon-γ production against CD105-expressing targets (**Extended Data Fig. 8**). Critically, the functional ranking did not mirror the apparent recombinant or cell-surface binding ranking: CLEN24 did not exhibit the highest apparent binding potency, yet EN24 conferred the most productive anti-CAF response. The best CAR therefore came from a binder conventional metrics would have discarded, and the explanation had to lie after binding.

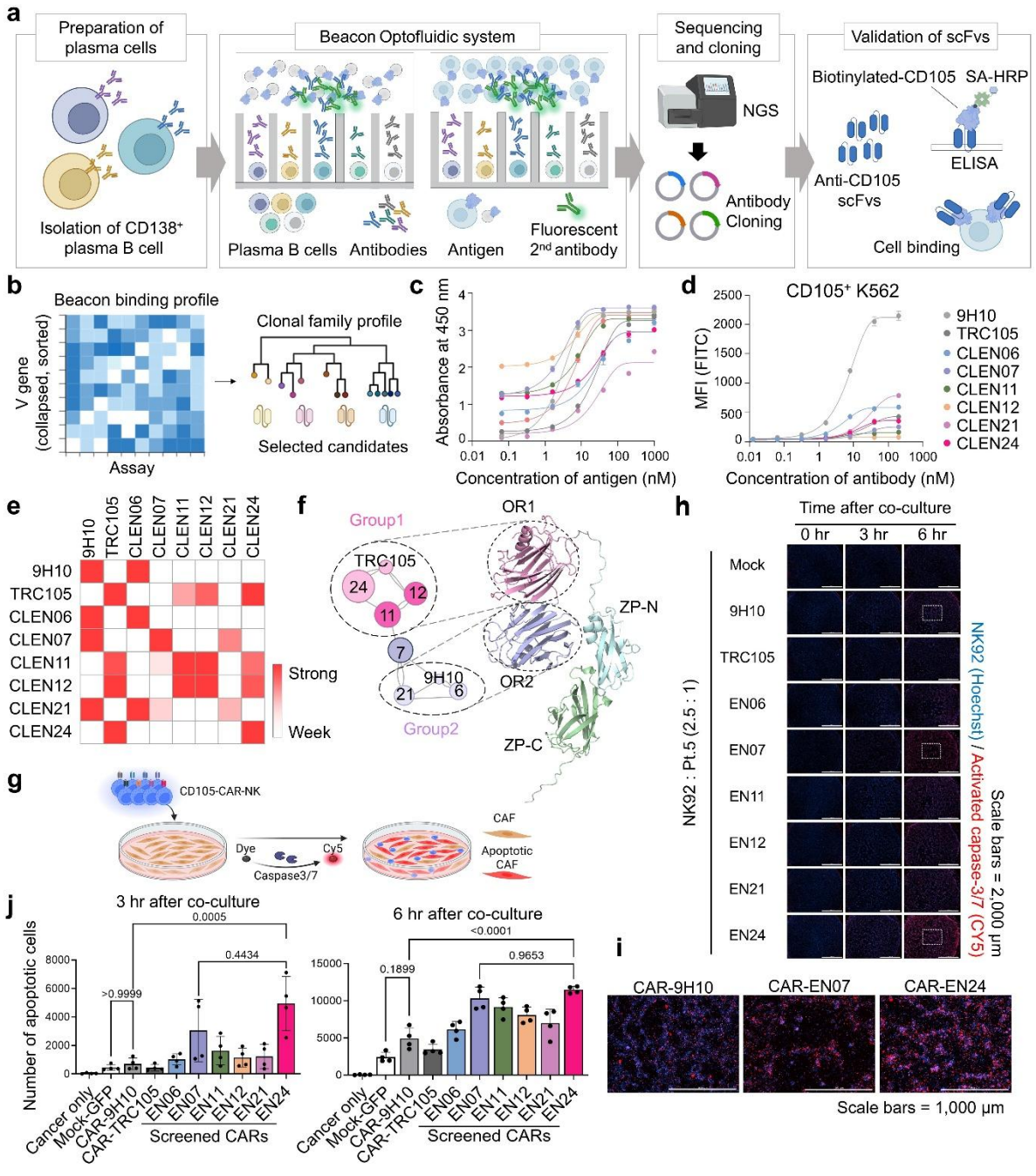


Fig. 3. A function-first screen identifies EN24, a binder that ranks low by binding potency yet builds the most productive CD105 CAR. a, Schematic of the plasma B-cell antibody discovery workflow using the Beacon optofluidic platform, followed by single-cell BCR sequencing, antibody cloning and recombinant scFv validation. **b,** Summary of CD105-specific

scFv candidate selection and prioritization. Representative candidates were selected across distinct clonal families and binding profiles and advanced together with the reference CD105 antibodies TRC105 and 9H10. **c,** ELISA binding of recombinant anti-CD105 scFvs against purified biotinylated CD105-His (n = 3 independent experiments). **d,** Flow cytometric scFv binding to surface CD105 on $CD105^+$ K562 cells, shown as FITC mean fluorescence intensity (MFI) (n = 3 independent experiments). **e,** Competitive epitope-binning heatmap of the prioritized scFvs (n = 3 independent experiments). **f,** Competition-guided structural mapping of the epitope groups onto an AlphaFold model of the CD105 ectodomain (residues 26–586). Prioritized antibodies were mapped to predicted binding regions, with CLEN24 resolved from the reference antibody 9H10. Structural regions include orphan (OR) domain 1 (residues 26–46 and 200–330, pink) and OR domain 2 (residues 47–199, purple), defined according to UniProt P17813, and the zona pellucida (ZP) module (residues 338–581; corresponding to the region resolved in PDB 5HZV), shown as its ZP-N (cyan) and ZP-C (green) subdomains. The OR–ZP linker (residues 331–337) and the membrane-proximal segment (residues 582–586), which immediately precedes the transmembrane helix and belongs to neither module, are shown in grey. All residues are numbered according to the full-length *ENG* precursor. **g,** Schematic of the image-based CAR-NK-92 functional screen using $CD105^+$ patient-derived CAFs (Pt.5) as targets and an activated caspase-3/7 dye (effector-to-target (E:T) ratio 2.5:1). **h,** Representative time-course images of CAF apoptosis after co-culture with NK-92 cells expressing the indicated CD105-targeted CARs. NK-92 cells and caspase-$3/7^+$ apoptotic CAFs are shown in blue and red, respectively. Scale bars, 2,000 μm. **i,** Higher-magnification images of CAF apoptosis induced by selected CD105-targeted CAR-NK-92 cells. Scale bars, 1,000 μm. **j,** Quantification of apoptotic CAFs after 3 h and 6 h of co-culture with the indicated constructs (n = 4). Data are mean ± s.d. unless otherwise indicated. P values were determined

using one-way ANOVA with Tukey's multiple comparisons.

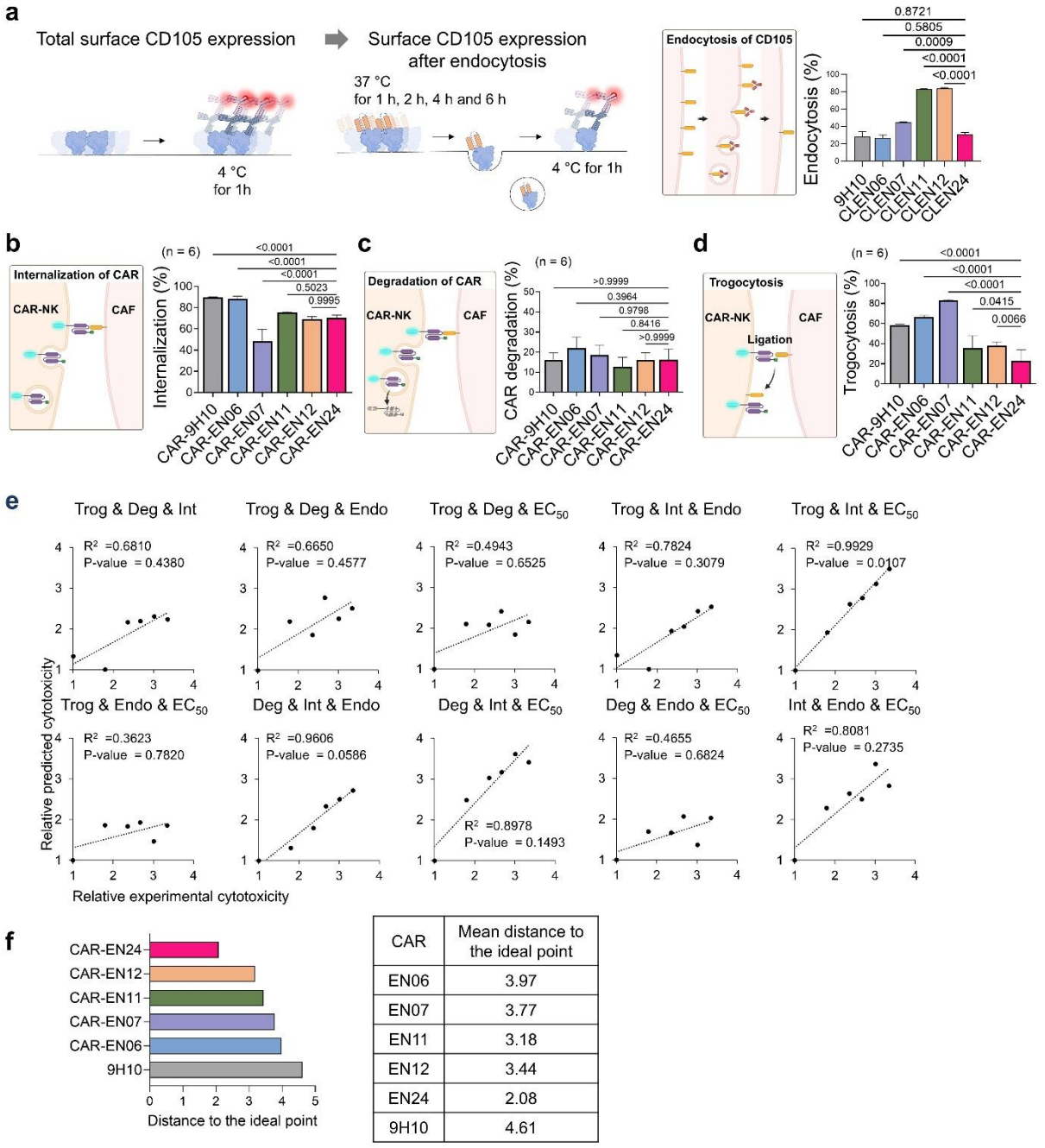
Post-engagement handling, not binding strength, points to the post-killing phase

Because static binding potency could not explain construct productivity, we profiled post-engagement receptor and antigen dynamics. We first examined antibody-induced CD105 endocytosis, which varied markedly among binders (**Fig. 4a and Supplementary Fig. 7**): CLEN11 and CLEN12 induced comparatively high internalization, CLEN24, 9H10 and several others less.

We next quantified three CAR-associated processes after co-culture of CD105-CAR-pNK cells with $CD105^{+}$ CAFs: loss of surface CAR through internalization, degradation of the CAR-associated fluorescent reporter, and trogocytosis-mediated acquisition of CD105 by effector cells (**Fig. 4b–d and Supplementary Fig. 8**). Each scFv conferred a distinct profile (**Fig. 4b,c**). Trogocytosis was the most binder-dependent of the three: EN06 and EN07 promoted substantial CD105 transfer, whereas EN24 induced the lowest level of any construct (**Fig. 4d**). The antigen-binding domain therefore governs not only recognition but the subsequent handling of both CAR and antigen.

Univariate regression showed that no single feature, including CD105 endocytosis, was associated with measured CAR-NK cytotoxicity (**Supplementary Fig. 9a**). Combinations did better. Across the six constructs profiled, models pairing CAR internalization with trogocytosis and either CD105 endocytosis or apparent binding potency showed the strongest associations with measured cytotoxicity (**Fig. 4e and Supplementary Fig. 9b,c**), indicating that productive

311 anti-CAF activity tracks coordinated post-engagement behaviour rather than any single feature.
312 A composite Euclidean-distance score across all five standardized features, calculated relative
313 to a reference profile comprising the most favourable observed value for each feature, ranked
314 EN24 first, well ahead of every other construct including 9H10 (**Fig. 4f**). Both analyses
315 converge on the construct that the functional screen had already singled out, and both point to
316 the post-engagement phase rather than binding strength as the place where EN24 and 9H10
317 diverge.



CAR	Mean distance to the ideal point
EN06	3.97
EN07	3.77
EN11	3.18
EN12	3.44
EN24	2.08
9H10	4.61

Fig. 4. Binder-dependent post-engagement CAR dynamics exclude single-feature explanations and point to the phase after target engagement. a, Schematic and quantification of antibody-induced CD105 endocytosis in CD105-positive target cells treated with the indicated CD105-specific antibodies ($n = 3$ independent experiments). **b–d,** Schematic

and quantification of surface CAR internalization (**b**), CAR degradation (**c**) and trogocytosis-mediated CD105 acquisition (**d**) in pNK cells expressing the indicated CD105-targeted CARs after co-culture with CD105-positive CAFs ($n = 6$ from 2 independent experiments). **e,** Selected three-parameter ordinary least-squares regression models relating combinations of post-engagement CAR-dynamic features and apparent binding potency (EC_{50}) to measured cytotoxicity. Relative model-predicted cytotoxicity is plotted against relative experimental cytotoxicity ($n = 6$ CAR constructs: EN06, EN07, EN11, EN12, EN24 and 9H10; each point is one independent replicate). Dashed lines indicate linear regression fits, and coefficients of determination (R^2) and P values are shown. **f,** Integrated post-engagement profile of each CD105-CAR construct. CD105 endocytosis, CAR internalization, CAR degradation, trogocytosis and apparent binding potency were Z-score standardized and directionally aligned, and each construct was scored by its mean Euclidean distance from a reference profile built from the most favourable observed value of each feature ($n = 6$ CAR constructs). Shorter distances indicate more favourable integrated post-engagement dynamics. Because the reference is derived from the observed data, the ranking is descriptive. Data are mean ± s.d. P values were determined by one-way ANOVA with Tukey's multiple comparisons.

EN24 kills at the same rate as 9H10 but disengages and resets far faster

Surface plasmon resonance showed that CLEN24 dissociated from CD105 about 11-fold faster than 9H10 (k_{off} 2.3×10^{-3} versus 2.1×10^{-4} s^{-1}), which bound with 40-fold higher affinity (K_D 0.5 versus 20.4 nM) (**Fig. 5a and Supplementary Fig. 10**). Despite this, force-based detachment analysis showed that EN24-CAR-NK cells retained sufficient cell-level avidity for

CD105-positive targets, albeit with a lower binding-force distribution than 9H10-CAR-NK cells (**Fig. 5b**). EN24 therefore balances productive engagement against faster release rather than maximizing antigen residence time.

EN24-CAR-pNK cells reduced the residual area of patient-derived CAFs more effectively than mock-pNK and 9H10-CAR-pNK cells after 24 h (**Fig. 5c**) and showed robust CD107a upregulation after CAF engagement (**Fig. 5d**). Consistent with CD105-dependent recognition, they preferentially killed CD105-expressing AsPC-1 cells while showing limited activity against parental CD105-low cells (**Supplementary Fig. 11**).

Live-cell imaging resolved the cellular consequences. The interval from CAR engagement to killing was comparable between EN24- and 9H10-CAR-pNK cells, but EN24-CAR-pNK cells disengaged more rapidly afterwards, with shorter killing-to-CAR-off and total CAR-on-to-CAR-off intervals (**Fig. 5e and Supplementary Videos 5, 6**). Killing and release are therefore separable phases of CAR function. EN24 does not kill faster but becomes available for the next target sooner. Live-cell confocal imaging showed efficient microtubule-organizing centre (MTOC) polarization towards the immune synapse for both constructs, but more rapid MTOC depolarization and detachment after killing for EN24-CAR-pNK cells (**Fig. 5f and Supplementary Fig. 12**). Together with the reduced trogocytosis observed in **Fig. 4**, these findings define EN24 as a reusable effector characterized by rapid post-killing disengagement and synapse reset.

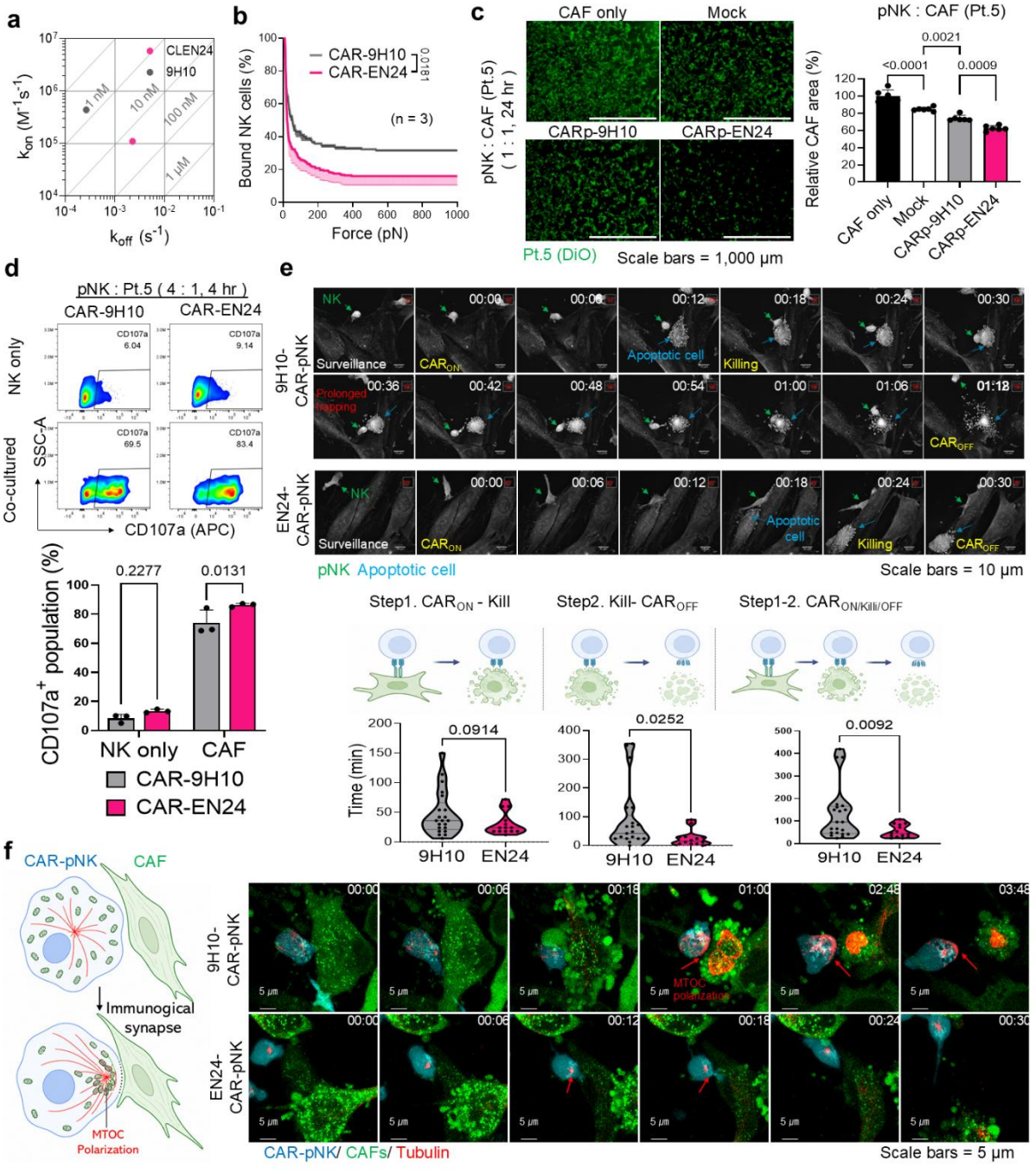


Fig. 5. EN24-CAR-NK cells kill at the same rate as 9H10-CAR-NK cells but release the killed target and reset the immune synapse more rapidly. a, SPR kinetic map showing association and dissociation rate constants of CLEN24 and 9H10 for CD105 ($n = 3$ independent experiments). CLEN24: $k_{on} = 1.1 \pm 0.1 \times 10^5$ M^{-1} s^{-1}, $k_{off} = 2.3 \pm 0.3 \times 10^{-3}$ s^{-1}, $K_D = 20.4 \pm 0.2$ nM; 9H10: $k_{on} = 4.5 \pm 0.3 \times 10^5$ M^{-1} s^{-1}, $k_{off} = 2.1 \pm 0.01 \times 10^{-4}$ s^{-1}, $K_D = 0.5 \pm 0.03$ nM.

b, Force-based cellular avidity analysis of 9H10- and EN24-CD105-CAR-NK cells interacting with CD105-positive target cells (n = 3 independent experiments). **c,** Representative fluorescence images and quantification of residual patient-derived CAFs after co-culture with mock-, 9H10-CAR- or EN24-CAR-pNK cells at an E:T ratio of 1:1 for 24 h (n = 6). CAFs are shown in green. Scale bars, 1,000 μm. **d,** Representative flow-cytometric plots and quantification of CD107a expression in 9H10- and EN24-CAR-pNK cells cultured alone or with patient-derived CAFs at an E:T ratio of 4:1 for 4 h (n = 3). **e,** Representative time-lapse images and quantification of CAR engagement dynamics during interactions with CD105-positive CAFs (n = 21 for 9H10 and n = 14 for EN24, single-cell resolution; three independent replicates). Engagement intervals were defined as CAR-on to killing, killing to CAR-off and total CAR-on to CAR-off. Green and blue arrows indicate CAR-pNK cells and apoptotic CAFs, respectively. Scale bars, 10 μm. **f,** Schematic and representative live-cell confocal images of MTOC polarization and reset during CAR-pNK–CAF interactions. CAR-pNK cells, CAFs and tubulin are shown in blue, green and red, respectively. Red arrows indicate MTOC localization. Scale bars, 5 μm. Data are mean ± s.d. P values were determined using two-way ANOVA for panel b, one-way ANOVA for panel c and unpaired two-tailed t-test for panel e.

Humanized EN24 (hEN24)-CAR-NK cells are reusable effectors that open an access window for a second therapy

We next tested whether faster post-killing disengagement improved repetitive target elimination. In serial-challenge assays, EN24-CAR-pNK cells maintained higher cytotoxicity than the slower-off 9H10-CAR-pNK cells across four consecutive rounds of target exposure (**Fig. 6a**). Activity declined for both constructs with repeated challenge, but the advantage of

EN24 was retained throughout.

We humanized CLEN24 by complementarity-determining region grafting onto human frameworks with structure-guided back-mutation (**Extended Data Fig. 9a**). Screening identified several variants retaining recombinant and cell-surface CD105 recognition (**Extended Data Fig. 9b–e and Supplementary Tables 3 and 4**). The lead framework-reverted clone, CLhEN24-12 (hEN24 as a CAR), preserved CD105 binding and a rapid dissociation profile by SPR (**Extended Data Fig. 9f**). It also retained the parental CAR on/off phenotype in primary NK cells (**Extended Data Fig. 10**). hEN24-based CARs were expressed in pNK cells at levels comparable to parental EN24 and 9H10 CARs (**Fig. 6b**). Their cytotoxicity against CD105-expressing PANC-1 targets matched parental EN24 and exceeded 9H10 (**Fig. 6c**).

In multicellular spheroids of AsPC-1-mCherry cancer cells and HPPF-GFP left untreated or treated with mock-pNK or hEN24-CAR-pNK cells (**Fig. 6d and Supplementary Videos 7–9**), hEN24-CAR-pNK treatment preferentially reduced the HPPF-GFP compartment, because parental AsPC-1 cells express minimal surface CD105. The decline in fibroblast area was followed by restriction of AsPC-1 expansion, whereas both compartments continued to increase in untreated and mock-treated spheroids. This pattern is consistent with withdrawal of fibroblast-mediated support rather than direct killing of cancer cells.

Finally, we tested whether stromal depletion improved a subsequently administered tumour-directed product. Fibroblast-rich spheroids were generated from MSLN-expressing PANC-1-mCherry cells and HPPF-GFP, treated first with CD105-CAR-pNK cells and 24 h later with MSLN-CAR-pNK cells (**Fig. 6e, Supplementary Fig. 13 and Supplementary Videos 10–14**). MSLN-CAR-pNK monotherapy poorly controlled the tumour compartment in the presence of

417 an intact fibroblast layer, whereas CD105-CAR-pNK monotherapy depleted HPPFs but only
418 partially suppressed it. Sequential treatment reduced the fibroblast compartment comparably
419 to CD105-CAR-pNK alone while controlling the tumour compartment substantially better than
420 either monotherapy. First-wave CAF elimination therefore opens a transient access window,
421 defining hEN24-CAR-pNK cells as reusable stromal effectors that prepare the tumour for a
422 second wave.

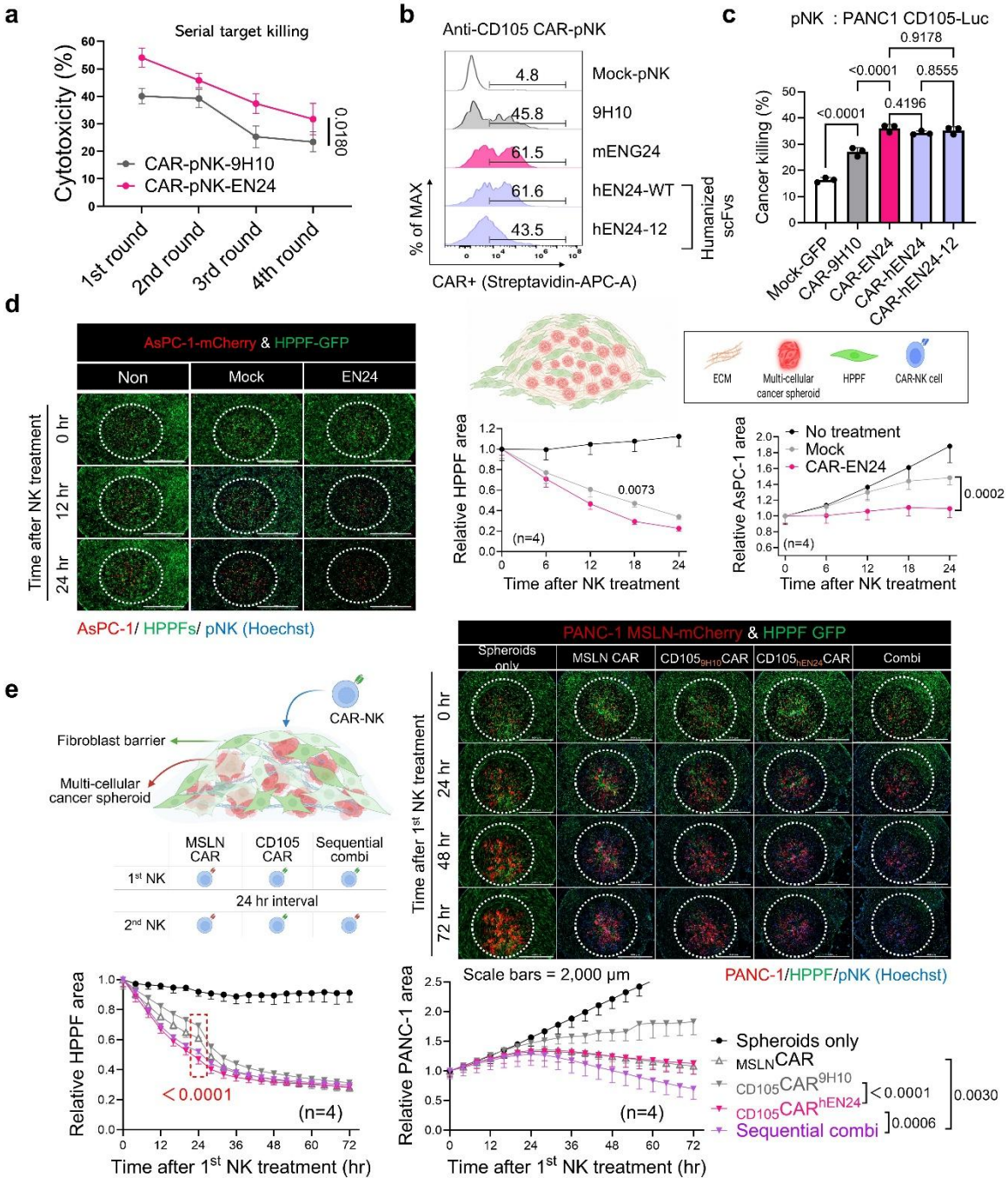


Fig. 6. Humanized EN24-CAR-NK cells act as reusable effectors and open an access window for tumour-directed CAR therapy in fibroblast-rich spheroids. a, Serial-killing activity of 9H10- and EN24-based CD105-CAR-pNK cells over four consecutive target-challenge rounds. Cytotoxicity was measured after each round ($n = 4$). **b,** Representative flow-cytometric histograms of surface CAR expression in mock-pNK cells and pNK cells expressing

9H10-, mouse EN24 (mEN24)- or the indicated humanized EN24 (hEN24)-based CD105 CARs, with percentages of CAR-positive cells. **c,** Cytotoxicity of the same effectors against CD105-expressing PANC-1-CD105-Luc cells (n = 3). **d,** Representative fluorescence images and quantification of HPPF and AsPC-1 tumour-cell areas in multicellular spheroids left untreated or treated with mock-pNK or hEN24-CAR-pNK cells (n = 4 spheroids per group). AsPC-1 cells, HPPFs and pNK cells are shown in red, green and blue, respectively. Dashed circles delineate spheroid boundaries. Scale bars, 2,000 μm. **e,** Schematic of sequential stromal priming in fibroblast-rich PANC-1-MSLN spheroids. CD105-CAR-pNK cells were administered as the first wave, followed 24 h later by MSLN-CAR-pNK cells. Representative fluorescence images and quantification of HPPF and PANC-1 tumour-cell areas are shown for untreated spheroids, MSLN-CAR-pNK monotherapy, 9H10- or hEN24-based CD105-CAR-pNK monotherapy and sequential combination treatment (n = 4 spheroids per group). PANC-1 cells, HPPFs and pNK cells are shown in red, green and blue, respectively. Scale bars, 2,000 μm. Data are mean ± s.d. P values were determined using two-way ANOVA for panels a, d, and e, and one-way ANOVA for panel c, followed by Tukey's multiple comparisons test.

hEN24-CAR-pNK priming opens an access window that admits and sustains tumour-directed CAR cells *in vivo*

We next asked whether this advantage was retained in fibroblast-rich tumours *in vivo*. AsPC-1-MSLN cells[14] and patient-derived CAFs were co-implanted subcutaneously into NSG mice. Mice then received mock-pNK, 9H10-CAR-pNK or hEN24-CAR-pNK cells intravenously (**Fig. 7a**). hEN24-CAR-pNK treatment delayed tumour growth relative to mock-pNK controls and to the slower-off 9H10-CAR-pNK comparator. Flow cytometry of dissociated tumours

showed a marked increase in intratumoural human CD45-positive cells after hEN24-CAR-pNK treatment (**Fig. 7b and Supplementary Fig. 14**), which persisted after normalization to tumour weight. The limited recovery of 9H10-CAR-pNK cells, despite recognition of the same antigen, suggests that binder-dependent post-engagement behaviour influences intratumoural effector access and persistence.

In a fibroblast-rich pancreatic tumour model, mice received MSLN-CAR-pNK cells alone or sequential hEN24-CD105-CAR-pNK followed by MSLN-CAR-pNK cells (**Fig. 7c**). MSLN-CAR-pNK monotherapy produced only partial tumour control, whereas sequential treatment suppressed growth substantially more, with more consistent individual trajectories. To ask whether priming extended beyond a CAR-NK-to-CAR-NK sequence, we administered hEN24-CD105-CAR-pNK cells before MSLN-directed CAR-T cells (**Fig. 7d and Supplementary Fig. 15a**). Sequential treatment improved tumour control over CD105-CAR-pNK monotherapy, establishing that the sequence is feasible across cell-therapy platforms. Because this model carried no MSLN-CAR-T monotherapy arm, we tested the priming contribution itself in a model that did.

We co-implanted MSLN-expressing AsPC-1 cells and patient-derived CAFs into the pancreas and included both single-agent controls, mock-pNK priming followed by MSLN-CAR-T and hEN24-CD105-CAR-pNK priming followed by mock T cells (**Fig. 7e**). Against both controls, the sequential combination improved tumour control by longitudinal bioluminescence imaging and *ex vivo* analysis (**Fig. 7e,f and Supplementary Fig. 15b**), isolating the contribution of stromal priming. Priming increased the numbers of $hCD45^+$ cells recovered from tumours, including both $hCD3^+hCD56^-$ T cells and $hCD3^-hCD56^+$ NK cells (**Fig. 7g**), and a higher proportion of the recovered T cells were MSLN-CAR-positive at endpoint (**Fig. 7h and**

Supplementary Fig. 16).

Because CD105 is expressed in non-malignant stromal and vascular compartments, we assessed systemic tolerability in human *ENG* knock-in (h*ENG* KI) NKG mice, in which the human-specific hEN24 CAR can engage host CD105. CAR-NK-treated mice showed a transient decrease in body weight followed by recovery towards baseline, and endpoint serum biochemistry showed no substantial treatment-related abnormalities relative to control animals (**Supplementary Fig. 17**). Together, these findings support a sequential mechanism in which stromal priming increases intratumoural immune-cell accumulation, sustains the MSLN-CAR-T compartment and improves tumour control. (**Fig. 8**).

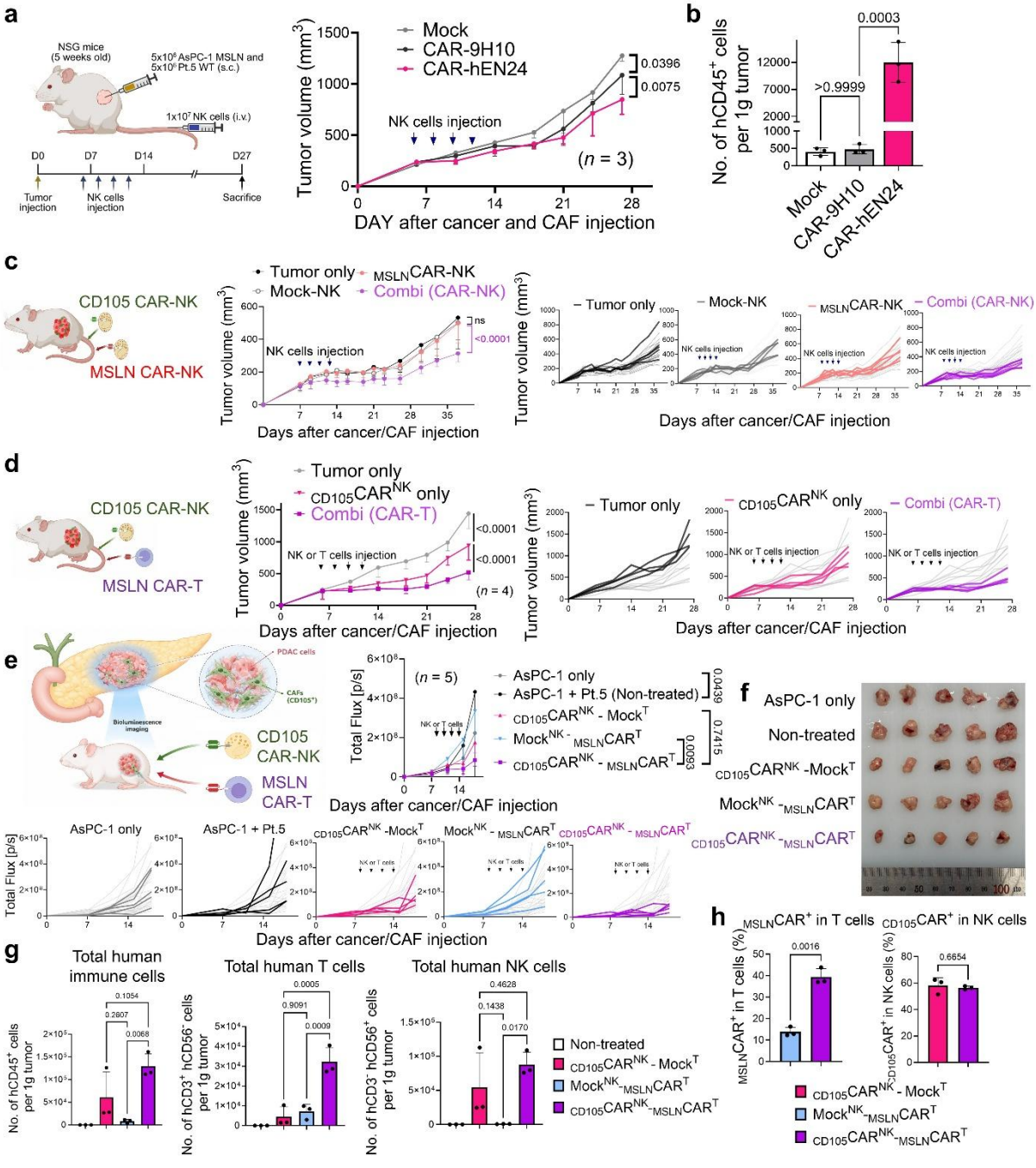


Fig. 7. hEN24-CAR-NK stromal priming opens an access window that admits tumour-directed cells, sustains the CAR-T compartment and improves tumour control *in vivo*. a, Schematic of the fibroblast-rich subcutaneous xenograft model and treatment schedule. AsPC-1-MSLN cells and patient-derived CAFs were co-implanted subcutaneously, followed by

intravenous administration of mock-, 9H10-CAR- or hEN24-CAR-pNK cells. Right, tumour-growth curves for mock-pNK, 9H10-CAR-pNK and hEN24-CAR-pNK groups (n = 3 mice per group). **b,** Representative flow-cytometric plots and quantification of intratumoural human CD45-positive cells recovered from the indicated groups, normalized to tumour weight (n = 3 mice per group; individual plots in **Supplementary Fig. 14**). **c,** Schematic and therapeutic evaluation of sequential CD105-CAR-NK stromal priming followed by MSLN-CAR-pNK therapy in PANC-1-MSLN/HPPF tumours. Tumour-growth curves are shown for tumour-only, mock-pNK, MSLN-CAR-pNK and sequential combination groups. Right panels show individual trajectories (Combination group, n = 6; all other groups, n = 5 mice). **d,** Schematic and therapeutic evaluation of sequential CD105-CAR-pNK priming followed by MSLN-CAR-T-cell therapy. Mean and individual tumour-growth curves are shown for tumour-only, CD105-CAR-pNK monotherapy and sequential combination groups (n = 4 mice per group). **e,** Schematic and therapeutic evaluation of an orthotopic PDAC model established by co-implantation of AsPC-1-MSLN-Luc cells and patient-derived CAFs into the pancreas, followed by sequential hEN24-CD105-CAR-pNK and MSLN-CAR-T therapy. Left, model schematic and treatment schedule. Right, longitudinal bioluminescence imaging and quantification of tumour burden (n = 5 mice per group). Lower panels show individual trajectories. **f,** Representative *ex vivo* image of tumours collected at the endpoint. **g,** Quantification of tumour-infiltrating total human immune cells ($hCD45^+$), T cells ($hCD3^+hCD56^-$) and NK cells ($hCD3^-hCD56^+$) in orthotopic tumours, normalized to tumour weight (n = 3 mice per group). **h,** Quantification of MSLN-CAR-positive tumour-infiltrating T cells and CD105-CAR-positive tumour-infiltrating NK cells (n = 3 mice per group). Arrows in **a**, **c**, **d** and **e** indicate the timing of NK- or T-cell administration. MSLN-CAR-NK cells express the SS1 anti-MSLN scFv and MSLN-CAR-T cells the anti-MSLN clone 10 (**Methods**). Data

are mean ± s.d. *P* values were determined using two-way ANOVA for panels a, c, d and e and one-way ANOVA for panels b, g and h followed by Tukey's multiple comparisons test.

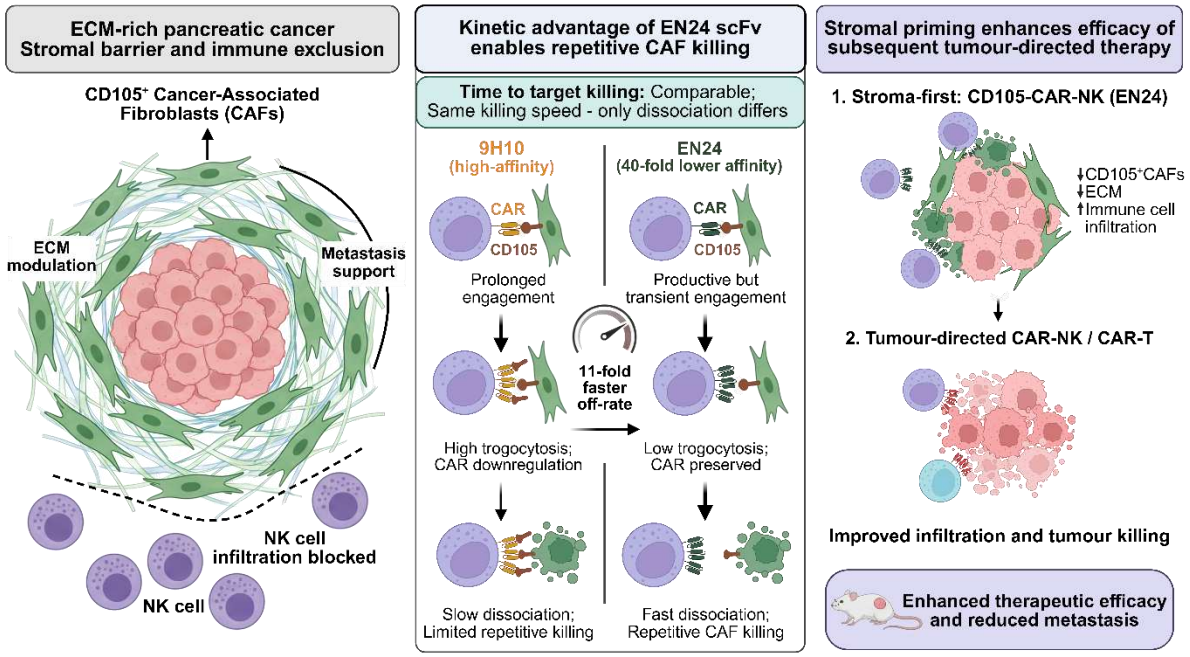


Fig. 8. Selecting for faster CAR–antigen disengagement enables repetitive stromal targeting and potentiates tumour-directed cellular immunotherapy. Schematic summary of the study. In ECM-rich PDAC, TGF-β-associated CD105-positive CAFs promote ECM remodelling and limit intratumoural NK-cell accumulation. Compared with the higher-affinity, slower-off 9H10 binder, EN24 supports sufficient antigen engagement but faster post-killing dissociation, reduced trogocytosis and CAR loss, accelerated immune-synapse resolution and MTOC reset, and sustained repetitive CAF killing. EN24-based CD105-CAR-NK cells consequently deplete CAFs in matrix-rich spheroids and, in fibroblast-rich tumours, increase intratumoural immune-cell accumulation and enhance the activity of a second wave of tumour-directed MSLN-CAR-NK or CAR-T cells.

Discussion

We developed a kinetically selected CAR-NK strategy that uses CAF depletion as a first-wave stromal-priming intervention for fibroblast-rich PDAC. Single-cell, spatial and functional analyses identified *ENG* as a marker and functional regulator of a TGF-β-associated, fibronectin-rich fibroblast state linked to adverse outcome, and *ENG* disruption reduced fibroblast motility, matrix gene expression, cancer-cell invasion and transendothelial migration, and increased intratumoural NK-cell accumulation.

The principal engineering insight is that the suitability of a CAR binder for repetitive stromal targeting cannot be inferred from binding potency alone. Plasma B-cell screening generated scFvs with diverse sequence, epitope and binding profiles, but their recombinant binding rank did not predict CAR-NK activity: CLEN24 did not exhibit the highest apparent binding potency, yet EN24 conferred the most productive anti-CAF activity. Integrated profiling placed EN24 in a favourable overall CAR-dynamic state, with the lowest trogocytosis among the constructs tested. SPR showed an 11-fold faster off-rate than the higher-affinity 9H10 binder. Live-cell imaging then localized the difference: EN24 did not kill faster but released the killed target far sooner, becoming available for reuse.

These findings support an engagement–reset model in which the CAR–antigen interaction is stable enough to support synapse formation, MTOC polarization, degranulation and target death, yet transient enough to permit rapid synapse resolution afterwards. This refines the conventional emphasis on maximal affinity: excessively persistent engagement may increase antigen extraction, receptor internalization or degradation and retain effectors on spent targets, whereas overly transient binding may fail to establish a cytolytic synapse. The optimal binder

therefore occupies a kinetic window that balances engagement against post-killing release. This balance should matter most for stromal targeting, where few effectors must repeatedly eliminate many non-malignant targets distributed through a dense matrix. Previous work has shown that serial killing by CAR-T cells depends on efficient detachment and receptor preservation[31-34], that functional avidity and antigen density set activation thresholds[35-37], and that immune-synapse organization and MTOC positioning regulate cytotoxic efficiency[38, 39]. Our findings extend these principles to CAR-NK-mediated stromal targeting.

The therapeutic consequence is a two-wave architecture. Humanization preserved the CD105 recognition and faster-off properties of CLEN24, and hEN24-CD105-CAR-pNK cells depleted fibroblasts in spheroids and increased NK-cell accumulation in CAF-rich xenografts. As monotherapy these cells primarily remodelled the stromal compartment rather than targeting CD105-low cancer cells. That distinction proved useful, because first-wave CAF depletion opened an access window for subsequently administered MSLN-directed cells. This modularity separates two functions that are difficult to optimize within a single product and may extend to other desmoplastic tumours in which antigen expression is adequate but cellular immunotherapy is limited by fibroblast expansion and immune exclusion.

Several limitations apply. First, the therapeutic studies used immunodeficient xenografts, which permit controlled evaluation of human CAFs and NK cells but do not reproduce adaptive immunity, myeloid suppression or patient-specific stromal heterogeneity. Second, CD105 is also expressed in endothelial and other non-malignant compartments. Administration of hEN24-CD105-CAR-pNK cells to h*ENG* KI mice caused only a transient, reversible body-weight change without substantial serum biochemical abnormalities, but defining antigen-density thresholds for normal-cell recognition will require dedicated biodistribution and

vascular-integrity studies. Third, the optimal timing, dose and duration of the priming window remain to be defined, and stromal depletion after priming has not yet been measured directly in treated tumours. Finally, CLEN24 and 9H10 differ in epitope and geometry as well as in kinetics. A matched series of CLEN24 variants with systematically altered off-rates would isolate the contribution of the off-rate itself and define its optimal range, and would test whether the engagement–reset principle generalizes to other CAF antigens and platforms.

In summary, we establish $CD105^{+}$ CAFs as functional drivers of an ECM-rich stromal niche that limits intratumoural NK-cell accumulation and identify CAR–antigen disengagement kinetics as an engineering variable for repetitive stromal targeting. Humanized EN24-CAR-NK cells exploit this property as reusable first-wave effectors that open an access window for subsequent CAR-NK or CAR-T therapy.

Methods

Ethical approval

Mouse immunization was performed in accordance with a protocol approved by the Institutional Animal Care and Use Committee (IACUC) of Seoul National University (protocol number SNU-220224-1-1). Breeding and maintenance of human *ENG* knock-in (h*ENG* KI) mice were performed under a separate protocol approved by the IACUC of Seoul National University (protocol number SNU-240806-7-5). All other *in vivo* experiments, including every xenograft efficacy study and the on-target/off-tumour tolerability study, were performed under a protocol approved by the IACUC of the Korea Institute of Science and Technology (protocol number KIST-2024-079). Analyses using human-derived clinical specimens and associated

research materials were performed under the approval of the Institutional Review Board of Asan Medical Center (IRB No. 2022-1493), and written informed consent was obtained from all participants. All experiments involving human-derived samples were conducted in accordance with the approved study protocol and relevant institutional and ethical guidelines.

Cell culture

HPPFs were obtained from Cell Biologics and cultured in DMEM supplemented with 10% fetal bovine serum (FBS), 1% antibiotic–antimycotic solution, 1% GlutaMAX and hFGF (10 ng ml^{-1}; PeproTech, 100-18B). HUVECs were obtained from Lonza and cultured in EGM Endothelial Cell Growth Medium BulletKit (Lonza, CC-3124) according to the manufacturer's instructions. The pancreatic cancer cell lines PANC-1, AsPC-1 and Capan-2 were purchased from the Korean Cell Line Bank (Seoul, Republic of Korea). PANC-1 cells were cultured in DMEM with 10% FBS and 1% antibiotic–antimycotic solution; AsPC-1 and Capan-2 cells were maintained in RPMI-1640 with 10% FBS, 1% antibiotic–antimycotic solution and HEPES (10 mM; Gibco, 15630080). NK-92 and HEK293T cells were purchased from the American Type Culture Collection (ATCC). HEK293T cells were cultured in DMEM with 10% FBS, 1% antibiotic–antimycotic solution and HEPES (10 mM). NK-92 cells were cultured in MEMα (Gibco, 12561-056) with 20% FBS, 10× MEM vitamin solution (Gibco, 11120-052), 2-mercaptoethanol (0.1 mM; Gibco, 21985023), 1% penicillin–streptomycin and rIL-2 (200 IU ml^{-1}; R&D Systems, 202-IL). K562 cells were purchased from the ATCC and cultured in RPMI-1640 (Welgene) with 10% FBS (Gibco) and 1× penicillin–streptomycin (Gibco). All cells were maintained at 37 °C with 5% CO_2 and were routinely confirmed to be free of mycoplasma using the e-Myco plus Mycoplasma PCR Detection Kit (Intron Biotechnology, 25237).

618

619 **Peripheral blood-derived NK cells and primary CAFs**

620 Primary NK cells were expanded from frozen peripheral blood mononuclear cells (PBMCs;
621 Lonza) for 2 weeks as previously described[13, 14]. Patient-derived pancreatic CAFs were
622 obtained from Asan Medical Center (Seoul, Republic of Korea) and maintained in RPMI-1640
623 supplemented with 10% FBS, 1% antibiotic–antimycotic solution and hFGF (1 ng ml^{-1}).

624 **Yeast strains and culture conditions**

625 Two *Saccharomyces cerevisiae* strains, JAR200 (*MATa*, GAL1-AGA1::KanMX4 ura3Δ45
626 ura3-52 trp1 leu2Δ1 his3Δ200 pep4::HIS3 prb1Δ1.6R can1) and YVH10 (*MATα*, PDI::ADHII-
627 PDI-Leu2 ura3-52 trp1 leu2Δ1 his3Δ200 pep4::HIS3 prb1Δ1.6R can1 GAL), were used for
628 constructing and screening the yeast surface display Fab library. These strains were kindly
629 provided by Professor Yong-Sung Kim (Ajou University, Suwon, Republic of Korea).

630 The haploid yeast library was cultured in SDCAA medium (6.7 g l^{-1} yeast nitrogen base, 5 g
631 l^{-1} casamino acids, 14.7 g l^{-1} sodium citrate, 4.29 g l^{-1} citric acid monohydrate and 20 g l^{-1}
632 dextrose in deionized water). For JAR200 cultures, SDCAA was supplemented with 0.0002 g
633 l^{-1} uracil; for YVH10 cultures, 0.0004 g l^{-1} tryptophan was added. The diploid Fab library was
634 cultured in SDCAA medium without these supplements. To induce Fab expression, the library
635 was sub-cultured in 2× SGCAA medium (13.4 g l^{-1} yeast nitrogen base, 10 g l^{-1} casamino acids,
636 5.4 g l^{-1} Na_2HPO_4, 8.56 g l^{-1} $NaH_2PO_4 \cdot H_2O$ and 20 g l^{-1} galactose) at an initial OD_{600} of 0.5
637 and incubated at 20 °C with shaking at 160 rpm for 48 h.

638

639 **Single-cell RNA-sequencing (scRNA-seq) data processing**

Publicly available scRNA-seq data from patients with PDAC were obtained from Werba et al.[30] (PMID: 36781852). The dataset included tumour samples from 27 patients, comprising 20 treatment-naïve and 7 chemotherapy-treated cases; treated patients had received FOLFIRINOX- or gemcitabine/abraxane-based chemotherapy before tissue acquisition. Raw count matrices were processed using the Seurat package (version 5.4) in R (PMID: 37231261). Quality control removed low-quality cells and potential doublets. Filtering thresholds for nCount and nFeature were determined using an interquartile range (IQR)-based approach, in which outliers were defined as values below the first quartile − 1.5 × IQR or above the third quartile + 1.5 × IQR. Cells with fewer than 200 detected genes or mitochondrial transcript proportions above 20% were excluded. Thresholds were determined separately for the treatment-naïve and chemotherapy-treated cohorts. Normalization and variance stabilization were performed per sample using SCTransform. Principal component analysis was performed on highly variable genes, followed by UMAP for dimensionality reduction. To minimize batch effects, anchor-based integration using canonical correlation analysis was performed with the IntegrateLayers function in Seurat. Clusters were identified by graph-based clustering using FindNeighbors and FindClusters. Major cell-type identities were assigned using representative marker genes reported in the original study, including T/NK cells (*CCL5*, *GNLY*, *NKG7*), epithelial cells (*KRT19*, *TFF1*), endothelial cells (*VWF*, *SPARCL1*), myeloid cells (*SPP1*, *APOE*), proliferating epithelial cells (*UBE2C*, *CCNB1*), proliferating lymphoid cells (*MKI67*, *CENPF*), proliferating myeloid cells (*MMP9*, *CTSK*), mast cells (*TPSAB1*, *KIT*), B/plasma cells (*IGKC*, *IGLC2*) and fibroblasts (*COL1A1*, *COL1A2*, *DCN*).

Cell-type identification and subclustering of CAFs

Cluster identities were assigned using marker genes from the original publication: epithelial

(*TFF1*, *LCN2*, *KRT19*, *SPINK1*, *TFF2*), myeloid (*SPP1*, *APOE*, *S100A9*, *IFI30*, *HLA-DRA*), fibroblast (*COL3A1*, *COL1A2*, *COL1A1*, *SFRP2*, *DCN*), T/NK (*CCL5*, *GNLY*, *NKG7*, *CCL4*, *IL7R*), endothelial (*SPARCL1*, *ACKR1*, *CCL14*, *VWF*, *COL4A1*), proliferating epithelial (*UBE2C*, *AKR1C2*, *UBE2S*, *CCNB1*, *S100A2*), proliferating lymphoid (*HIST1H4C*, *HMGB2*, *STMN1*, *MKI67*, *CENPF*), B/plasma (*IGKC*, *IGLC2*, *IGHG1*, *IGLC3*, *IGLC1*), proliferating myeloid (*MMP9*, *CTSK*, *ACP5*, *CST3*, *RGS10*) and mast (*TPSAB1*, *TPSB2*, *CPA3*, *MS4A2*, *KIT*).

Gene Set Enrichment Analysis (GSEA)

Fibroblasts were classified as ENG-positive (ENG^+) or ENG-negative (ENG^-) based on ENG transcript expression in normalized expression matrices. Cells with detectable ENG expression (expression value > 0) were defined as ENG^+ fibroblasts, while those lacking detectable expression were defined as ENG^- fibroblasts. GSEA was performed separately in treatment-naïve and chemotherapy-treated patients with PDAC. For the cell-level analysis, gene ranking was generated using Wilcoxon rank-sum statistics implemented in the presto package (version 1.0.0). Differential gene expression between ENG^+ and ENG^- fibroblasts was calculated using the wilcoxauc function, and genes were ranked using the area under the curve (AUC)-derived scores [sign(logFC) × AUC]. To account for potential donor-level pseudoreplication, GSEA was additionally performed using a donor-level pseudobulk approach [PMID: 34584091]. Within each donor, raw UMI counts were aggregated separately for ENG^+ and ENG^- fibroblasts, and only donors containing both populations were included in the paired analysis. Pseudobulk count matrices were analysed using edgeR (version 4.4.2), with lowly expressed genes filtered using filterByExpr and library-size normalized using the trimmed mean of M-values (TMM) method [PMID: 19910308]. Donor identity was included as a blocking factor in the design

matrix, and the ENG^+ vs ENG^- effect was estimated using a quasi-likelihood negative binomial generalized log-linear model. Genes were ranked according to the signed quasi-likelihood test statistic, and the resulting ranked gene list was used for donor-level GSEA. Gene sets were obtained from the Molecular Signatures Database (MSigDB) using the msigdbr package (version 26.1.0). Hallmark gene sets (collection H) were used as the primary reference and pathways associated with stromal activation and ECM remodelling were specifically evaluated, including GOBP_EXTRACELLULAR_MATRIX_ASSEMBLY, GOBP_POSITIVE_REGULATION_OF_EXTRACELLULAR_MATRIX_ORGANIZATION. GSEA was performed using the fgsea package (version 1.30.0) with 1,000 permutations (nPermSimple = 1000). Results were summarized by the normalized enrichment scores (NES), nominal p-values, and false discovery rates (FDR).

Analysis of differentially expressed genes

Differentially expressed genes between ENG^+ and ENG^- fibroblasts were identified using the FindMarkers function in Seurat following SCT normalization with PrepSCTFindMarkers. Significant genes were defined as those with an adjusted P value < 0.01 and absolute $\log_2$ fold change ≥ 0.25.

Spatial transcriptomics profiling and analysis

Formalin-fixed paraffin-embedded tumour tissues from 36 patients were prepared as tissue microarrays. Representative tumour cores identified by pathologists (36 cores from 36 patients, one core per patient) were analysed using the Visium Spatial Gene Expression platform for FFPE samples (10x Genomics). Sequencing data were processed using Space Ranger (10x Genomics; RRID:SCR_025848) followed by a Scanpy-based pipeline[40]. During quality control, low-quality spots were removed based on gene counts and mitochondrial transcript ratios, and

batch effects between slides were corrected using Harmony integration[41].

Cell-type composition of each spatial spot was estimated using CellDART[42] with a publicly available PDAC scRNA-seq reference. CAF regions were defined using the CellDART-based CAF annotation, integrating deconvolution fractions with subtype assignments (myCAF-like, iCAF-like, apCAF-like and other CAFs). As a sensitivity analysis, an alternative CAF mask was generated using a fibroblast gene signature (*COL3A1*, *COL1A2*, *COL1A1*, *SFRP2*, *DCN*), yielding consistent results. Within CAF regions, *ENG*$^{+}$ CAF spots were defined as spots with *ENG* expression greater than or equal to the median *ENG* expression across CAF spots within each region.

Spatial relationships between tumour, stromal and immune populations were quantified using the STopover spatial topological overlap index[43]. *ENG*$^{+}$ CAF regions were used as the anchor, and co-localization with tumour subtype, CAF subtype, ECM and immune signatures was quantified using the composite Jaccard index. Pathway activity and transcriptional programmes were calculated using PROGENy[44] and curated gene sets. Spatial ligand–receptor interactions were evaluated using the stLearn spot-level permutation framework[45]. Activity scores were averaged across *ENG*$^{+}$ CAF spots within each tumour core and summarized across samples. For visualization, the highest-ranking ligand–receptor pairs were selected within biologically curated signalling categories, including the TGF-β axis and ECM–integrin signalling.

Survival analysis

Overall survival (OS) was assessed according to *ENG* expression in basal-like tumour spots identified by spatial transcriptomic analysis. Among the 36 patients included in the spatial transcriptomic cohort, 21 patients with basal-like tumour spots were included in the survival analysis. For each patient, mean *ENG* expression was calculated across the designated basal-

like tumour spots, and patients were stratified into *ENG*-high and *ENG*-low groups using the median patient-level *ENG* expression as the cut-off. Kaplan–Meier survival curves were generated and compared using a two-sided log-rank test, and hazard ratios (HRs) with 95% confidence intervals (CIs) were estimated using a univariable Cox proportional hazards regression model with *ENG* expression group as the sole covariate. Statistical analyses were performed in Python 3.12.11 using the lifelines package (version 0.30.3). Kaplan–Meier estimates, log-rank tests and Cox regression were performed using KaplanMeierFitter, lifelines.statistics.logrank_test and CoxPHFitter, respectively[46]. The Breslow method was used for baseline hazard estimation, with Efron handling of tied event times. All statistical tests were two-sided, and $P < 0.05$ was considered statistically significant.

Western blot analysis

Cells were lysed in RIPA buffer supplemented with sodium fluoride, sodium orthovanadate, sodium pyrophosphate and a protease inhibitor cocktail (Roche). Lysates were mixed with sample buffer, separated by SDS–PAGE and transferred onto polyvinylidene difluoride membranes. Membranes were blocked with skim milk for 30 min at room temperature, then incubated overnight at 4 °C with the following primary antibodies: β-actin (Santa Cruz Biotechnology, 1:2,000), CD105 (R&D Systems, 1:1,000), α-SMA (Proteintech, 1:1,000), E-cadherin (ABclonal, 1:1,000), fibronectin (Abcam, 1:2,000), vimentin (ABclonal, 1:1,000) and COL1A1 (ABclonal, 1:1,000). Membranes were then incubated with horseradish peroxidase (HRP)-conjugated secondary antibodies, and proteins were detected using a ChemiDoc system (Bio-Rad). Uncropped images of all blots are provided in **Supplementary Fig. 2.**

Immunofluorescence staining for TGF-β1-induced CD105 expression

To confirm upregulation of CD105 by TGF-β1 (10 ng ml^{-1}; BioLegend, 781804), TGF-β1-

755 treated HPPFs were fixed with 4% paraformaldehyde for 10 min and permeabilized with 0.1%
756 Triton X-100 in phosphate-buffered saline (PBS) for 10 min at room temperature. Cells were
757 blocked with 2.5% bovine serum albumin (BSA) in PBS for 30 min at room temperature and
758 incubated with primary antibodies against CD105 (R&D Systems, 1:250) and β-actin (Santa
759 Cruz Biotechnology, 1:1,000) overnight at 4 °C with rotation. Primary antibodies were
760 aspirated, cells were washed twice with DPBS and stained with mouse IgG Alexa Fluor 647
761 and goat IgG Alexa Fluor 488 secondary antibodies (Abcam) at room temperature for 1 h.
762 Nuclei were counterstained with Hoechst 33342 (5 μg ml^{-1}; Thermo Fisher Scientific).
763 Fluorescence images were captured on a BioTek Lionheart FX automated live-cell imager
764 (Agilent Technologies) and quantified using Gen5 software (Agilent Technologies).

765 **CRISPR–Cas9-mediated knockout of *ENG* in fibroblasts**

766 To generate *ENG*-knockout fibroblasts, 2×10^6 cells were electroporated with a mixture of 4
767 μg recombinant Cas9 protein (IDT, 1081059) and 0.4 nmol synthetic single guide RNA
768 targeting *ENG* (sgRNA sequence 5′-GGACTTCAAGGATGGCATTG-3′; IDT) using a Neon
769 Transfection System 100 μl kit (Invitrogen, MPK10096) at 1,700 V (20 ms, one pulse). Control
770 fibroblasts were electroporated using the same protocol with Cas9 protein alone and without
771 sgRNA, and are referred to throughout as Cas9-only control fibroblasts. After electroporation,
772 cells were transferred into pre-warmed complete medium and cultured for 48 h. Loss of CD105
773 was assessed by flow cytometry and western blot analysis.

774 **CAF motility assay using live-cell holotomography**

775 Live-cell holotomography imaging was performed on an HT-X1 system (Tomocube). The
776 system was equipped with a 450 nm light-emitting diode source, a 40× motorized objective
777 (NA 0.95) and a condenser lens (NA 0.72; working distance 30 mm). Illumination patterns

were modulated using a digital micromirror device, and three-dimensional refractive index tomograms were acquired across multiple axial planes using TomoStudio X software (Tomocube). CAFs were seeded into 24-well plates at 1×10^4 cells per well and incubated overnight before imaging. During time-lapse imaging, cells were maintained at 37 °C and 5% CO_2 using a stage-top incubator (Tokai Hit). Focus was maintained using a 780 nm laser-based autofocus system, and reconstructed tomograms were generated using deconvolution-based image reconstruction software. For quantitative motility analysis, time-lapse datasets were converted into maximum-intensity projection images and imported into Aivia AI Image Analysis Software v14 (Leica Biosystems). Cells were detected and tracked across sequential frames using the Cell Tracking tool in the Recipe Console, and tracking outputs were used to extract mean velocity.

Invasion and transendothelial migration assays

Assays were performed using 24-well Transwell inserts with 8 μm-pore polycarbonate membranes (Corning, 3422). For the invasion assay, 2×10^5 fibroblasts were seeded in the lower chamber and incubated overnight; the upper chamber was coated with Matrigel (0.5 mg ml^{-1}; Corning, 354248) and allowed to solidify for 30 min at 37 °C. Then 5×10^4 cancer cells suspended in serum-free medium were seeded into the coated upper chambers and incubated for 24 h. For the transendothelial migration assay, 1×10^5 HUVECs were seeded in the upper chamber to form a confluent monolayer on the day of fibroblast seeding, and 5×10^4 DiO-labelled (Invitrogen, V22886) cancer cells suspended in serum-free medium were added on top of the endothelial monolayer and allowed to migrate for 24 h at 37 °C. Non-migrated cells were removed from the upper membrane surface with a cotton swab, followed by two DPBS washes. Invaded or transmigrated cells on the underside of the membrane were fixed with 4%

paraformaldehyde and stained with Hoechst 33342 (Thermo Fisher Scientific) for 10 min at room temperature. Membranes were washed twice with DPBS, imaged on a BioTek Lionheart FX imager and quantified using Gen5 software.

Quantitative real-time PCR

Total RNA was extracted using TRIzol reagent (Thermo Fisher Scientific, 15596026) according to the manufacturer's instructions. cDNA was synthesized from 5 μg of total RNA using a cDNA Reverse Transcription kit (Enzynomics, RT200), which accepts up to 5 μg of input RNA per reaction. Quantitative PCR was performed using a SYBR Green qPCR PreMIX kit (Enzynomics, RT500M) on a QuantStudio instrument (Thermo Fisher Scientific). Primer pairs were: *GAPDH* (forward 5′-CAGCCTCAAGATCATCAGCA-3′; reverse 5′-TGTGGTCATGAGTCCTTCCA-3′), *VIM* (forward 5′-AGGTGGACCAGCTAACCAAC-3′; reverse 5′-CTCCTCCTGCAATTTCTCCC-3′), *COL1A1* (forward 5′-CCTGGATGCCATCAAAGTCT-3′; reverse 5′-CGCCATACTCGAACTGGAAT-3′) and *FN1* (forward 5′-AGTAAACCTGAAGCTGAAGAGACT-3′; reverse 5′-GCATGATCAAAACACTTCTCAGCTA-3′). Relative mRNA levels were calculated using the $\Delta\Delta C_t$ method and normalized to *GAPDH*.

Preparation of recombinant proteins

To express CD105-His and CD105-wtFc (residues 26–586), CD105 genes were synthesized by IDT and cloned into the pcDNA3.4 mammalian expression vector by Gibson assembly. Protein expression was performed in Expi293 cells; His-tagged CD105 proteins were purified by Ni-NTA affinity chromatography and wtFc-fused CD105 proteins by protein A resin (Amicogen) affinity chromatography. After elution, buffer exchange was performed and purity was confirmed by SDS–PAGE. Recombinant CD105 was biotinylated using the EZ-Link Sulfo-

NHS Biotinylation Kit (Thermo Fisher Scientific).

Mouse immunization

Under IACUC protocol SNU-220224-1-1, six-week-old female BALB/c mice were immunized intraperitoneally every two weeks with 50 μg CD105-His protein suspended in 50% (v/v) aluminium hydroxide adjuvant. Blood samples were collected weekly, and sera were obtained by centrifugation for determination of anti-CD105 antibody titres. For ELISA, 96-well Maxisorp microplates (Thermo Fisher Scientific) were coated with 100 ng CD105-His per well and incubated overnight at 4 °C. Wells were blocked for 1 h at room temperature with 1× PBS (pH 7.4) containing 3% BSA and washed three times with PBST (PBS with 0.05% Tween 20). Mouse sera were serially diluted ten-fold, added to the wells and incubated for 1 h at room temperature. After washing, HRP-conjugated goat anti-mouse IgG (H+L) (Invitrogen) was added at 1:8,000 and incubated for 1 h. Plates were washed, developed with 3,3′,5,5′-tetramethylbenzidine (TMB) substrate and stopped with 2 M H_2SO_4. Absorbance at 450 nm was recorded on an Infinite 200 PRO NanoQuant microplate reader (Tecan).

Selection of antigen-specific plasma B cells using an optofluidic device

Mouse plasma B cells were isolated using a $CD138^+$ Plasma Cell Isolation Kit (Miltenyi Biotec) and an Opto Plasma B Discovery Sample Prep Kit, Mouse (Bruker, formerly Berkeley Lights), and loaded onto OptoSelect 20k chips in a Beacon optofluidic system (Bruker). Single-cell penning was performed using optoelectronic positioning technology, which uses light to guide individual plasma B cells into discrete NanoPens.

Three on-chip fluorescence-based assays were used to identify cells secreting anti-CD105 antibodies. For the recombinant CD105 binding assay, biotinylated CD105-wtFc proteins were

incubated with assay beads (Bruker) and loaded into OptoSelect 20k chips alongside Alexa Fluor 488-conjugated AffiniPure $F(ab')_2$ goat anti-mouse IgG (H+L) (Jackson ImmunoResearch) at 1:500. For the cell-surface CD105 binding assay, CD105-positive K562 reporter cells were used to detect binding to native CD105. To detect antibody secretion, goat anti-mouse IgG beads (Spherotech) were used to monitor overall antibody production.

Anti-CD105 antibody-secreting plasma cells were lysed directly in NanoPens for cDNA synthesis using an OptoSeq Barcoded BCR kit (Bruker), then exported to individual wells of a 96-well plate for cDNA amplification PCR using the same kit. Antibody heavy- and light-chain sequences were amplified using an OptoSeq Barcoded BCR NGS library prep kit (Bruker). BCR amplicons were pooled and processed with a Nextera XT library preparation kit (Illumina). Final libraries were sequenced on an Illumina MiSeq platform, and the resulting data were analysed using primeseq, which identified the closest matching V and J gene segments at the nucleotide level.

Beacon image processing, bloom quantification and heatmap visualization

Assay images captured on the Beacon platform were exported in PDF format, parsed using the pypdf library and converted into NumPy arrays for downstream digital image processing. Individual-well regions of interest were isolated based on predefined Cartesian coordinates to generate image tiles per well. Handwritten specimen identifiers were decoded using a k-nearest neighbours classifier (k = 3; scikit-learn) trained on a curated, manually annotated dataset, with feature vectors reduced to three principal components before classification. Target feature detection was performed by evaluating the normalized inner product between a reference template and the query image against an empirical fixed threshold. After automated grid registration, bloom intensity was determined by counting pixels exceeding a specified intensity

threshold within paired regions of interest. The compiled data matrix was rendered as a heatmap using matplotlib and seaborn with a consistent colour scale across all experimental groups. Workflows were implemented in Python (v3.11); source code availability is described under Code availability.

Single-cell antibody repertoire profiling and clonal characterization

Single-cell antibody repertoire sequences were annotated using IgBLAST against the IMGT mouse germline reference database. Downstream filtration retained only productive rearrangements, defined as in-frame sequences without premature stop codons and with a fully qualified complementarity-determining region 3 (CDR3). CDR boundaries were defined according to IMGT conventions. Junctional nucleotide sequences were used to calculate CDR3 amino acid lengths, which were modelled for heavy (IGH) and light (IGK/IGL) chains by kernel density estimation using matplotlib and seaborn in Python (v3.11). Sequences were grouped into clonal clusters on the basis of shared IGHV and IGHJ gene usage together with IGH CDR3 length and similarity (**Extended Data Fig. 6a**). A single representative was then advanced from each cluster for recombinant scFv expression, so that clonally redundant sequences were excluded from downstream characterization regardless of their reactivity in the primary screen. Antibody sequences were analysed using IgBLAST (version 1.22.0) and subsequently clustered based on identical V and J gene assignments and equal CDR3 lengths. Somatic hypermutation frequencies were assessed in R (v4.5.1) using the Immcantation framework (alakazam, shazam and scoper): V-gene regions were aligned to their predicted germline ancestors, and the somatic hypermutation rate was defined as the number of nucleotide mismatches per base within the aligned V region. Distributions were displayed using ggplot2 violin plots overlaid with boxplots showing the median and interquartile range. Data

892 restructuring and string operations used dplyr and stringr.

893 **Preparation of recombinant anti-CD105 scFv proteins**

894 Selected antibody genes were subcloned in frame into the pMopac12 vector using Gibson
895 assembly (NEB). The resulting scFv-pMopac12 plasmid was transformed into *Escherichia coli*
896 BL21(DE3) cells, which were cultured in 500 ml Terrific Broth supplemented with
897 chloramphenicol. Cultures were grown at 37 °C with shaking at 200 rpm to an OD_{600} of 0.6–
898 0.8, at which point expression was induced with 0.5 mM IPTG, and induced cultures were
899 incubated for a further 16 h at 25 °C with shaking at 160 rpm. Cells were harvested by
900 centrifugation at 10,000*g* for 20 min and resuspended in 32 ml Tris–sucrose solution (100 mM
901 Tris, 0.75 M sucrose; pH 7.5). Lysozyme was added to a final concentration of 20 mg/mL, and
902 the suspension was incubated at 4 °C with agitation. Cells were then treated with 1 mM EDTA
903 (pH 8.0). The periplasmic fraction was collected by centrifugation and filtration, and His-
904 tagged scFv proteins were purified by affinity chromatography. Purity was assessed by 12%
905 SDS–PAGE.

906 **ELISA detection of anti-CD105 scFvs**

907 Binding activities of anti-CD105 scFvs were assessed by ELISA. Each well of a 96-well
908 Maxisorp microplate was coated with 100 ng scFv and incubated overnight at 4 °C. After
909 blocking with 1× PBS containing 3% BSA for 1 h at room temperature, five-fold serially
910 diluted biotinylated CD105-His or CD105-wtFc antigen was added and incubated at room
911 temperature for 1 h, followed by washing with PBST. Streptavidin–HRP (Abcam, ab7403,
912 1:40,000) or HRP-conjugated goat anti-human IgG Fc secondary antibody (Invitrogen,
913 1:12,000) was then added and incubated for 1 h at room temperature. After washing, TMB
914 substrate was added and the reaction stopped with 2 M H_2SO_4. Absorbance at 450 nm was

measured on a microplate reader (Tecan). EC_{50} values were derived from these curves. For competitive ELISA, either 200 nM biotinylated CD105-His alone or a preformed complex of 200 nM biotinylated CD105-His and 400 nM anti-CD105 scFv was used. Competition was determined by normalizing the absorbance of the antigen-only sample to 100% and expressing experimental absorbance as a percentage of that baseline.

Cell binding assay of anti-CD105 scFvs

CD105-positive and CD105-negative K562 cells (5×10^4 per well) were resuspended in PBSF in a 96-well round-bottom plate and centrifuged at 300*g* for 3 min. Pellets were washed once with fresh PBSF. Recombinant anti-CD105 scFvs at various concentrations were added, and cells were incubated at 4 °C for 1 h. Cells were washed in PBSF and incubated with anti-His-FITC (Abcam, ab1206, 1:400) at 4 °C for 15 min. After a final PBSF wash, cells were analysed by flow cytometry to quantify scFv binding, and EC_{50} values were derived from the resulting curves.

Construction of lentiviral vectors

To construct plasmids encoding CAR genes, all DNA fragments, including anti-CD105 scFv candidates, the CAR construct and GFP, were amplified by PCR using specific primers. Each fragment was cloned as a second-generation CAR (scFv–CD8 hinge–CD8 transmembrane–4-1BB–CD3ζ) into the pCDH lentiviral vector (Addgene, 72266) using a NEBuilder HiFi DNA assembly kit (New England Biolabs, E2621L) according to the manufacturer's protocol.

MSLN-targeted CAR construct

Two mesothelin (MSLN)-directed CAR constructs were used in this study. Both are second-generation CARs incorporating an anti-MSLN scFv (SS1 for NK cells or Clone10 for T cells),

together with a CD3ζ signalling domain, and both were cloned into the lentiviral backbone and transduced as described below. MSLN-CAR-NK cells **(Fig. 6e, Fig. 7c and Supplementary Fig. 13b)** carry the SS1 anti-MSLN scFv[14], whereas MSLN-CAR-T cells **(Fig. 7d-h and Supplementary Fig. 15a)** carry the anti-MSLN clone 10[28]. CAR expression was confirmed by flow cytometry before each experiment. Because the second-wave product was tested with two independent MSLN binders, the priming effect reported here is not attributable to a single tumour-directed binder.

Production of lentivirus encoding CARs or expression DNA

To produce lentiviruses, the expression vector encoding CARs or antigens, the psPAX2 packaging vector and a baboon envelope vector (for NK cells) or VSV-G envelope vector (for cancer cells or T cells) were mixed with polyethylenimine (Polysciences, 23966-1) in Opti-MEM (Gibco, 11058-021). The mixture was incubated at room temperature for 20 min and transfected into HEK293T cells. Lentivirus supernatants were collected once daily for 2 days and concentrated using a Lenti-X concentrator (Takara, 631232) according to the manufacturer's protocol.

Generation of CAR-NK and CAR-T cells

CAR-NK-92 cells were transduced with lentivirus at a multiplicity of infection (MOI) of 100 in the presence of polybrene (10 μg ml^{-1}; Merck, TR-1003); CAR-pNK cells were transduced at an MOI of 10 using Vectofusin-1 (10 μg ml^{-1}; Miltenyi Biotec, 130-111-163); and CAR-T cells were transduced at an MOI of 10 in the presence of polybrene (10 μg ml^{-1}). CAR expression was confirmed by GFP expression or by staining with the corresponding biotinylated antigen (human CD105 or MSLN) followed by streptavidin (BD Pharmingen), and analysed by flow cytometry.

Generation of genetically engineered cell lines

To establish the reporter cell lines used in this study, cancer cells were transduced with lentivirus containing an expression vector and a selection marker in the presence of polybrene (10 μg ml^{-1}). After 48 h, puromycin (InvivoGen, ant-pr-1) or geneticin (Gibco, 10131-035) was added to eliminate untransduced cells. Transduction efficiency was assessed by flow cytometry.

Flow cytometric analysis

Flow cytometry was performed on a CytoFLEX flow cytometer (Beckman Coulter Life Sciences) or a FACSCanto II (BD Biosciences), and data were analysed using FlowJo v10.9 (BD Biosciences). Dead cells were excluded using Fixable Viability Dye eFluor 506 or eFluor 780 (Thermo Fisher Scientific). Surface CD105 was detected using a PE-conjugated anti-human CD105 antibody. Antibodies and staining conditions for individual assays are described in the corresponding Methods sections and listed in the Reporting Summary.

Flow-cytometric analysis of NK-cell activation markers

For degranulation, 4×10^4 target cells (cancer cells or patient-derived CAFs, as indicated) were seeded per well of a 96-well plate and NK cells were added at a 4:1 effector-to-target (E:T) ratio with APC-conjugated anti-CD107a antibody (BioLegend) and GolgiStop protein transport inhibitor (BD Pharmingen) for 4 h. NK cells were then collected and stained with PE-conjugated anti-CD56 antibody (BioLegend). For IFN-γ staining, 4×10^4 target cells were seeded per well, NK cells were added at a 4:1 E:T ratio with GolgiStop (BD Biosciences, 554724) and incubated for 4 h. NK cells were collected, stained with PE-conjugated anti-CD56 antibody (BioLegend), then fixed and permeabilized using IC Fixation Buffer (eBioscience,

00-8222-49) and Permeabilization Buffer (eBioscience, 00-8333-56) and stained with APC-conjugated anti-IFN-γ antibody (BioLegend) according to the manufacturer's instructions.

Luminescence-based evaluation of cancer cell killing

Briefly, 4×10^4 cancer cells expressing Nano-Luciferase were seeded into 96-well plates overnight and co-cultured with NK cells at the indicated E:T ratios for 24 h. To assess remaining cancer cells, dead cells were washed out with DPBS and adherent cells lysed with RIPA buffer (Thermo Fisher Scientific). Debris was removed by centrifugation, and supernatants were used to detect luminescence with the Nano-Glo Luciferase Assay System (Promega, N1120) according to the manufacturer's instructions.

Serial-killing (repetitive challenge) assay

AsPC-1-CD105-Luc target cells were seeded at 4×10^4 cells per well in 96-well plates one day before co-culture. CD105-CAR-pNK cells were added at an effector-to-target ratio of 1:1 and co-cultured for 48 h. After each round, the effector cells were recovered and transferred with fresh culture medium onto newly seeded AsPC-1-CD105-Luc cells for the next round. Luciferase activity of the remaining target cells was measured after each round as described above, and cytotoxicity was calculated from the luminescence signal. Four sequential rounds were performed.

Endocytosis assay of anti-CD105 scFvs

CD105-positive K562 cells (5×10^4) were resuspended in PBS, aliquoted into a 96-well round-bottom plate and centrifuged at 300*g* for 3 min. Pellets were washed once with PBS before resuspension in complete RPMI-1640. Cells were treated with 50 nM anti-CD105 scFv and incubated at 37 °C in 5% CO_2 for 0, 1, 2, 4 and 6 h. Cells were washed with PBSF and incubated

with 50 nM anti-CD105 IgG antibody targeting a different epitope at 4 °C for 1 h. After another PBSF wash, PE-conjugated goat anti-human IgG Fc secondary antibody (1:400) was added and cells were incubated in the dark at 4 °C for 15 min. After a final PBSF wash, cell-surface CD105 was analysed by flow cytometry. The extent of endocytosis was determined as: endocytosis (%) = 100% − [(MFI of surface CD105 after endocytosis) / (MFI of total surface CD105 at 0 h, 37 °C) × 100%].

In silico structural analysis

To predict the three-dimensional structure of the CD105 extracellular domain, AlphaFold3 (Google DeepMind; PMID: 38718835) was used. The model with the highest predicted local distance difference test (pLDDT) score and predicted TM-score (pTM) was selected for further analysis. Structural comparisons were carried out in PyMOL (v3.1).

Assessment of CAR behaviour

Pt.5 cells (2×10^5) were seeded per well of a 24-well plate. CAR-pNK cells expressing a CFP-tagged intracellular domain were added at a 2:1 E:T ratio and co-cultured for 1 h. All cells were then harvested and washed with cold DPBS. Surface staining used biotin-conjugated anti-Myc antibody (BioLegend) and Fixable Viability Dye eFluor 780 (eBioscience), followed by secondary staining with streptavidin–APC (BD Biosciences) and FITC-conjugated anti-CD56 antibody (BioLegend). Trogocytosis was assessed as the proportion of $CD105^+$ cells within the CFP^+ CAR-pNK population. CAR internalization and degradation were quantified from fluorescence intensity changes as:

CAR internalization (%) = 100% − [(MFI of surface Myc^+ signal in co-cultured NK group) / (MFI of surface Myc^+ signal in NK only group) × 100%]

CAR degradation (%) = 100% − [(MFI of CFP^+ signal in co-cultured NK group) / (MFI of CFP signal in NK only group) × 100%]

Integrated analysis of CAR-dynamic features and NK-cell cytotoxicity

Throughout this study, apparent binding potency refers to ELISA- and cell-binding EC_{50} values, whereas affinity refers to SPR-derived K_D. To assess the relationship between CAR-associated features and NK-cell cytotoxicity, five quantitative parameters were measured for each CAR construct: apparent binding potency (EC_{50}), antibody-induced CD105 endocytosis, CAR internalization, CAR degradation and trogocytosis. Measurements from independent replicates were averaged for each construct before downstream analysis. Associations between individual features and cytotoxicity were first evaluated by Pearson correlation. Ordinary least-squares regression models were then constructed to determine whether combinations of features better explained cytotoxicity than single parameters. Candidate models containing up to three predictor variables were evaluated to limit model complexity given the number of constructs analysed. Because the models and the reference profile were both derived from these six constructs, the regression and the distance ranking are exploratory and were used to rank constructs rather than to predict cytotoxicity. For integrated comparison, each of the five construct-level feature values was then Z-score normalized across the six constructs. Based on an a priori designation of CD105 endocytosis, CAR internalization, CAR degradation and trogocytosis as cost features were directionally aligned by a factor of -1, ensuring that higher normalized values consistently represented more favorable properties. A reference CAR profile was constructed from the most favourable observed value of each aligned feature, and each construct's Euclidean distance from this reference was calculated as the square root of the sum of squared differences across the five aligned features. Constructs were ranked based on this

distance, with smaller values indicating more favourable integrated profiles. Analyses were performed in R v4.6.0 using the tidyverse v2.0.0 and Hmisc v5.2-3 packages.

Live-cell imaging-based evaluation

To evaluate killing activity, 2×10^4 Pt.5 cells were seeded into 96-well plates and stained with Vybrant DiO (Thermo Fisher Scientific). pNK cells stained with Hoechst 33342 (Thermo Fisher Scientific) were added to the pre-seeded CAFs at a 1:1 E:T ratio. Fluorescence images were captured at the indicated time points on a BioTek Lionheart FX imager (Agilent Technologies) and quantified using Gen5 software. For apoptosis analysis, 2×10^4 Pt.5 cells were seeded per well of a 96-well plate, and Hoechst-stained NK-92 cells were added at a 2.5:1 E:T ratio with CellEvent Caspase-3/7 Red Reagent (Invitrogen, 10431) at the recommended concentration. Apoptosis signal and fluorescence images were captured at the indicated times on the same instrument and quantified using Gen5 software.

Cell avidity assay

Pt.5 cells were seeded into poly-L-lysine-coated z-Movi chips (LUMICKS) and incubated for 30 min to allow attachment and reach 80% confluency. NK cells were labelled with Vybrant DiD Cell-Labeling Solution (5 µl per 1×10^6 cells; Invitrogen) according to the manufacturer's instructions. DiD-labelled CAR-NK cells (1×10^7 cells ml^{-1}) were injected into the chip (20 µl per test) and allowed to interact with the adherent target cells for 7 min. An acoustic force ramp from 0 to 1,000 pN was then applied over 2.5 min using a z-Movi Cell Avidity Analyzer (LUMICKS). Avidity was determined from the detachment profile, and the percentage of CAR-NK cells remaining bound at increasing force levels was quantified using z-Movi software (LUMICKS).

CAR ON/OFF assay using live-cell holotomography

Live-cell holotomography acquisition was performed on the HT-X1 system described in the CAF motility assay section. For CAR on/off analysis, CAFs were seeded into 24-well plates at 2×10^4 cells per well and incubated overnight before imaging, and CAR-NK cells were added immediately before the start of time-lapse acquisition. Images were acquired at 6 min intervals and monitored manually. CAR ON was defined as formation of an immunological synapse between an NK cell and a Pt.5 target cell; the killing time point was defined by the appearance of apoptotic bodies in NK-bound Pt.5 cells; and CAR OFF was defined as complete detachment of the NK cell from the apoptotic body.

Kinetics of microtubule-organizing centre (MTOC) polarization

For live-cell imaging of MTOC polarization, CAR-NK cells were labelled with Tubulin Tracker Deep Red (5 μM; Invitrogen, T34077) and CellTrace Violet (Invitrogen, 34571) for 30 min at 37 °C. Cells were washed with DPBS and added to Pt.5-GFP target cells seeded onto a glass-bottom confocal dish 24 h before imaging, at a 1:1 ratio. Time-lapse imaging was performed on a Stellaris 8 confocal microscope (Leica Microsystems) with a 100×/1.40 NA oil-immersion objective. Fluorophores were excited using a 405 nm diode laser and a tunable white light laser at 488 nm and 657 nm, and signals were collected using HyD detectors. Images were acquired as five z-stacks at 6 min intervals over 4 h, exported using LAS X software (Leica Microsystems) and analysed with Aivia software (Leica Microsystems).

Generation of three-dimensional multicellular spheroids

To generate 3D multicellular spheroids, a collagen solution was prepared to a final volume of 200 μl by mixing collagen (1.5 mg ml^{-1}; Corning, 354236), 20 μl of 10× PBS, 7.6 μl of 0.5 N

NaOH, 20 μl of cancer cells (2×10^6 cells ml^{-1}) and deionized water. The mixture was gently pipetted to ensure homogeneity, dispensed into each well of a 96-well plate and incubated in a CO_2 incubator for 30 min to solidify. HPPF-GFP cells were then seeded at 2×10^4 cells per 100 μl per well and incubated for 4 days. Hoechst-stained NK cells were added for the killing assay. For the sequential treatment assay, CD105-CAR-pNK cells were added as the first wave and MSLN-CAR-pNK cells 24 h later. Live-cell imaging was performed on a BioTek Lionheart FX imager and quantified using Gen5 software (Agilent Technologies).

Construction of a humanized antibody library

Murine antibody CDRs were grafted onto a human antibody framework. Guided by AlphaFold3 structural modelling, back-mutations were introduced into the humanized sequence to recapitulate key structural features of the original murine antibody, and a library incorporating both back-mutated variants and the humanized sequences was constructed for screening. Variable heavy (VH) and variable light (VL) gene segments were first PCR-fused to the CH1 and CL constant domains, respectively. The resulting VH-CH1 and VL-CL constructs were individually introduced into *S. cerevisiae* strains JAR200 and YVH10 by homologous recombination using linearized pYDS-H and pYDS-K vectors. Heavy- and light-chain libraries were merged by yeast mating to generate a Fab library displayed on the yeast cell surface for high-throughput screening of CD105-specific antibodies.

Screening of the humanized Fab library

To induce Fab expression, the library was initiated at an OD_{600} of 0.5 in 2× SGCAA medium and cultured at 20 °C with agitation at 160 rpm for 48 h. Surface expression was evaluated by immunolabelling the Flag epitope appended to the light-chain C terminus using a mouse anti-Flag antibody (Invitrogen, MA1-91878). A biotinylated antigen was then co-incubated with the

cells at room temperature for 1 h. Cells were washed with PBSA (PBS containing 0.1% BSA, pH 7.2), and secondary staining was performed at 4 °C for 15 min using FITC-conjugated anti-mouse IgG (Sigma-Aldrich, F0257) and SA-PE (Invitrogen, S866) after an additional PBSA wash. Cells were then analysed and sorted by flow cytometry using an SH800S cell sorter (Sony).

Surface plasmon resonance (SPR)

Anti-CD105 scFv binding kinetics were measured on a Biacore T200 instrument (Cytiva). Recombinant CD105 protein was immobilized onto CM5 sensor chips by amine coupling according to the manufacturer's instructions (Cytiva), and HBS-EP buffer (Cytiva, BR100669) was used as running buffer. Serial dilutions of anti-CD105 scFv were injected at 50 μl min^{-1} for 120 s, and dissociation was monitored for 5 min. The chip surface was regenerated with sequential 30 s injections of 50 mM glycine-HCl (pH 2.5) and 0.5 M arginine (pH 8.0). K_D values were determined using a 1:1 Langmuir binding model in Biacore T200 Evaluation (Cytiva). Results represent the mean of three independent experiments ($n = 3$).

Immunohistochemistry

CD105 expression in human PDAC tissues was assessed by immunohistochemistry using patient-derived PDAC tissue arrays provided by Asan Medical Center. Tissue sections were incubated at 60 °C for 30 min, deparaffinized, rehydrated and subjected to antigen retrieval using Epitope Retrieval Solution from the Bond Polymer Refine Detection Kit (Leica Biosystems, DS9800). After blocking, sections were incubated for 30 min with anti-CD105/endoglin rabbit monoclonal antibody (ABclonal, A19008-20; 1:5,000). Signals were developed using 3,3′-diaminobenzidine from the same kit, and slides were mounted and imaged on an Olympus BX53 microscope (Olympus).

Mouse xenograft studies

All xenograft experiments were conducted under IACUC protocol KIST-2024-079. Five-week-old male NOD.Cg-*Prkdc*^{scid} *Il2rg*^{tm1Wjl}/SzJ (NSG) mice were used for all efficacy studies described below. Mice were randomized before NK- or T-cell administration to equalize mean baseline tumour burden across groups.

To evaluate fibroblast-driven tumour growth *in vivo* (**Extended Data Fig. 2**), mice were subcutaneously co-inoculated with PANC-1-mCherry cells (2×10^6) and HPPFs (2×10^6). Tumour growth was monitored on an IVIS Spectrum imaging system (PerkinElmer) using filter settings appropriate for mCherry fluorescence.

To investigate the functional role of CD105$^+$ CAFs *in vivo* (**Fig. 2c–f**), mice were subcutaneously co-inoculated with AsPC-1 cells (5×10^6) and either *ENG*-KO or Cas9-only control CAFs (5×10^6). Forty-eight hours before sacrifice, 1×10^7 DiD-labelled primary NK cells were administered intravenously. Tumours and lungs were harvested for analysis of tumour-infiltrating NK cells and lung metastasis, respectively.

To evaluate the *in vivo* efficacy of hEN24-CD105-CAR-pNK cells (**Fig. 7a,b**), NSG mice were subcutaneously co-inoculated with AsPC-1-MSLN cells (5×10^6) and Pt.5 CAFs (5×10^6). After tumour establishment, NK cells (1×10^7) were administered intravenously four times at two-day intervals. At the endpoint, mice were sacrificed and tumours collected for analysis of tumour-infiltrating NK cells. Tumour tissues were dissociated using a human Tumor Dissociation Kit (Miltenyi Biotec, 130-095-929) on a gentleMACS Octo Dissociator (Miltenyi Biotec).

To assess sequential stromal priming followed by tumour-directed CAR therapy (**Fig. 7c,d**),

two independent xenograft models were established. For the sequential MSLN-CAR-NK model (**Fig. 7c**), NSG mice were subcutaneously co-inoculated with PANC-1-MSLN cells (2×10^6) and HPPFs (2×10^6). For the sequential MSLN-CAR-T model (**Fig. 7d**), NSG mice were subcutaneously co-inoculated with AsPC-1-MSLN cells (5×10^6) and Pt.5 CAFs (5×10^6). After tumour formation, mice received intravenous injections of CD105-CAR-pNK cells followed by either MSLN-CAR-pNK cells (1×10^7 per dose) or MSLN-CAR-T cells (3×10^6 per dose) at two-day intervals.

To evaluate sequential CD105-CAR-pNK and MSLN-CAR-T therapy in an orthotopic PDAC model (**Fig. 7e–h**), NSG mice were orthotopically implanted in the pancreas with AsPC-1-MSLN-Luc cells (2×10^6) together with Pt.5 CAFs (2×10^6). Tumour growth was monitored longitudinally by bioluminescence imaging on an IVIS Spectrum system (PerkinElmer). After tumour establishment, mice received intravenous injections of the respective NK cells (1×10^7) followed by the corresponding T cells (3×10^6) at two-day intervals. At the endpoint, mice were sacrificed and tumours collected for *ex vivo* imaging and dissociated using a human Tumor Dissociation Kit and a gentleMACS Octo Dissociator (Miltenyi Biotec). Single-cell suspensions were analysed by flow cytometry to quantify total human immune cells ($hCD45^+$) and, within the $hCD45^+$ population, human T cells ($hCD3^+hCD56^-$) and NK cells ($hCD3^-hCD56^+$), as well as CAR expression on tumour-infiltrating T and NK cells.

Flow-cytometric analysis of human CD105 expression in mouse lung endothelial cells

Human *ENG* knock-in (hENG KI) mice were generated on the severely immunodeficient NKG background (NOD.Cg-*Prkdc*^{scid} *Il2rg*^{em1Cya}/Cya) by Cyagen Biosciences (Suzhou, China) by CRISPR–Cas9-mediated replacement of part of the exon 1 coding region of mouse *Eng* (chromosome 2; 15 exons; transcript MGP_NODShiLtJ_T0053872) with a Kozak–human

ENG coding sequence–mouse *Eng* 3′ untranslated region–WPRE–bovine growth hormone polyadenylation signal cassette, placing human *ENG* under the control of the endogenous mouse *Eng* locus. Cas9 ribonucleoprotein complexes carrying two single guide RNAs (gRNA-A1, 5′-CGGGTGGACAGCATGGACCG-3′; gRNA-B1, 5′-AGACTCCCGGGTGGACAGCA-3′) were co-injected with the donor vector into fertilized oocytes; founders were confirmed by PCR and Sanger sequencing and backcrossed to wild-type NKG mice, and F1 offspring with stable germline transmission were used to establish the colony.

Lungs were harvested from hENG KI mice and wild-type NKG mice (n = 2 per genotype, 8 weeks of age, one male and one female per genotype), rinsed in complete DMEM (DMEM with 10% FBS and 1% antibiotic–antimycotic solution), trimmed of residual non-pulmonary tissue, washed in PBS and minced with scissors in a 60-mm dish. Minced tissue was digested in 5 ml collagenase/dispase (2 mg ml−1 in serum-free DMEM) for 45 min at 37 °C with agitation every 10 min, with DNase I (NEB, M0303L; 1:100 from a 4 mg ml−1 stock) added for the final 15 min. The digest was dissociated by repeated pipetting, passed through a 70-μm cell strainer and brought to 25 ml with complete DMEM and PBS. Cells were pelleted at 300g for 3 min, incubated in 5 ml of 1× red blood cell lysis buffer (BioLegend) for 5 min at 4 °C, quenched with complete DMEM and pelleted again.

Cells were counted and 1×10^6 cells per sample were washed in PBSF (PBS containing 0.5% BSA and 1 mM EDTA) and stained in 100 μl for 30 min at 4 °C with FITC anti-mouse CD45 antibody (30-F11, BioLegend; 1:200), anti-mouse CD31 (2H8, Invitrogen; 1:200) and the human CD105-specific human IgG antibody 9H10 (10 μg/mL). After washing in PBSF, cells were incubated for a further 30 min at 4 °C with Alexa Fluor® 647 AffiniPure® Goat Anti-

Armenian Hamster IgG (H+L) (127-605-160, Jackson ImmunoResearch; 1:200) and PE-conjugated anti-human IgG Fc (12-4998-82, Invitrogen; 1:200), washed, resuspended in 250 µl PBSF and analysed by flow cytometry.

Pulmonary endothelial cells were defined as $CD45^{-}CD31^{+}$ single cells, and human CD105 was quantified within this gate as the PE median fluorescence intensity. Because 9H10 recognizes human but not mouse CD105, lungs from wild-type NKG mice stained in parallel defined the background signal.

On-target/off-tumour toxicity assessment

To assess the on-target/off-tumour toxicity of CD105-CAR-NK cells, human ENG knock-in (hENG KI) mice were used. Heterozygous hENG KI mice aged 5–12 weeks, including both males and females, were randomly assigned to four treatment groups (n = 4 per group; two males and two females per group): vehicle control, mock-pNK, hEN24-CD105-CAR-pNK (5×10^6 cells) and hEN24-CD105-CAR-pNK (1×10^7 cells). The indicated NK-cell products were administered intravenously, and body weight was monitored longitudinally for 14 days. At the endpoint, blood was collected for serum biochemical analysis, and serum aspartate aminotransferase, alanine aminotransferase, blood urea nitrogen and creatinine were measured to assess potential hepatic and renal toxicity.

Statistics and reproducibility

Statistical analyses were performed using GraphPad Prism v10.4.2 and R v4.6.0. Unpaired two-tailed t-tests were used for comparisons between two groups. One-way ANOVA followed by Tukey's multiple comparisons test was used for comparisons among more than two groups. Two-way ANOVA followed by Tukey's multiple comparisons test was used for longitudinal

analyses, including tumour-growth curves and body weight change, except for the two-group longitudinal analysis in Extended Data Fig. 2, for which Šídák's multiple comparisons test was used. Overall survival was compared using a two-sided log-rank test. The test applied to each comparison is stated in the corresponding figure legend. Sample sizes were not predetermined by statistical methods and follow standard practice in the field: *in vitro* experiments used two to three technical replicates and were performed in at least two to three independent experiments, with the number of independent experiments specified in each figure legend, and *in vivo* experiments used 3–7 mice per group. No data were excluded from analysis. Mice were randomized to treatment groups before cell administration as described above. Investigators were not blinded to group allocation during data collection or analysis, because data collection and readout analysis were performed by the same personnel. For imaging-based quantification, the experimental unit is stated in each figure legend. All data are presented as the mean ± s.d. unless otherwise indicated.

Reporting summary

Further information on research design is available in the Nature Portfolio Reporting Summary linked to this article.

Data availability

The processed scRNA-seq dataset from Werba et al.[30] is publicly available at the Gene Expression Omnibus under accession number GSE205013. The spatial transcriptomic dataset analysed in this study was derived from a previously established cohort of patients with PDAC who underwent upfront surgery or neoadjuvant chemotherapy followed by resection; the present study is an independent secondary analysis focusing on $CD105^{+}$ fibroblast biology and spatial tumour–stroma interactions, which were not addressed in the original report. This

Visium dataset has not yet been deposited in a public repository because the primary description of the cohort is in preparation. Processed count matrices and spot-level annotations sufficient to reproduce every spatial analysis reported here are available to editors and reviewers on request, and the dataset will be deposited in the Gene Expression Omnibus at the time of publication of the primary report. Source data are provided with this paper. All remaining data supporting the findings of this study are available within the article and its Supplementary Information, or from the corresponding authors upon reasonable request.

Code availability

Custom code used for Beacon assay image processing, bloom quantification and heatmap visualization is available at Zenodo (https://doi.org/10.5281/zenodo.20805676). The R code used for the downstream single-cell RNA-seq analyses in this study is publicly available in the GitHub repository at the https://github.com/BI-research/pdac-eng-scrna GitHub repository and has been archived at Zenodo (https://doi.org/10.5281/zenodo.23050787).c

References

1. June, C.H., O'Connor, R.S., Kawalekar, O.U., Ghassemi, S. & Milone, M.C. CAR T cell immunotherapy for human cancer. *Science* **359**, 1361-1365 (2018).
2. Liu, E. et al. Use of CAR-Transduced Natural Killer Cells in CD19-Positive Lymphoid Tumors. *New England Journal of Medicine* **382**, 545-553 (2020).
3. Martinez, M. & Moon, E.K. CAR T Cells for Solid Tumors: New Strategies for Finding, Infiltrating, and Surviving in the Tumor Microenvironment. *Front Immunol* **10**, 128 (2019).
4. Joyce, J.A. & Fearon, D.T. T cell exclusion, immune privilege, and the tumor microenvironment. *Science* **348**, 74-80 (2015).

5. Sahai, E. et al. A framework for advancing our understanding of cancer-associated fibroblasts. *Nature Reviews Cancer* **20**, 174-186 (2020).
6. Kung, H.C., Zheng, K.W., Zimmerman, J.W. & Zheng, L. The tumour microenvironment in pancreatic cancer - new clinical challenges, but more opportunities. *Nat Rev Clin Oncol* **22**, 969-995 (2025).
7. Hosein, A.N., Brekken, R.A. & Maitra, A. Pancreatic cancer stroma: an update on therapeutic targeting strategies. *Nat Rev Gastroenterol Hepatol* **17**, 487-505 (2020).
8. Gok Yavuz, B. et al. Cancer associated fibroblasts sculpt tumour microenvironment by recruiting monocytes and inducing immunosuppressive PD-1(+) TAMs. *Sci Rep* **9**, 3172 (2019).
9. Jacobs, J. et al. Unveiling a CD70-positive subset of cancer-associated fibroblasts marked by pro-migratory activity and thriving regulatory T cell accumulation. *Oncoimmunology* **7**, e1440167 (2018).
10. Galluzzi, L., Chan, T.A., Kroemer, G., Wolchok, J.D. & López-Soto, A. The hallmarks of successful anticancer immunotherapy. *Sci Transl Med* **10**, eaat7807 (2018).
11. Cheng, Y. et al. Cancer-associated fibroblasts induce PDL1+ neutrophils through the IL6-STAT3 pathway that foster immune suppression in hepatocellular carcinoma. *Cell Death Dis* **9**, 422 (2018).
12. Malchiodi, Z.X. & Weiner, L.M. Understanding and Targeting Natural Killer Cell-Cancer-Associated Fibroblast Interactions in Pancreatic Ductal Adenocarcinoma. *Cancers (Basel)* **13**, 405 (2021).
13. Lee, Y.E. et al. Synergistic therapeutic combination with a CAF inhibitor enhances CAR-NK-mediated cytotoxicity via reduction of CAF-released IL-6. *J Immunother Cancer* **11**, e006130 (2023).
14. Shin, S.H. et al. An innovative strategy harnessing self-activating CAR-NK cells to mitigate TGF-β1-driven immune suppression. *Biomaterials* **314**, 122888 (2025).
15. Kang, S.B. et al. Enhancing cancer killing and natural killer cell persistence by targeting NOXA, a predictor of poor patient survival. *Mol Ther Oncol* **34**, 201152 (2026).
16. Pawlak, J.B. & Blobe, G.C. TGF-β superfamily co-receptors in cancer. *Dev Dyn* **251**, 137-163 (2022).
17. Paauwe, M. et al. Endoglin Expression on Cancer-Associated Fibroblasts Regulates

Invasion and Stimulates Colorectal Cancer Metastasis. *Clin Cancer Res* **24**, 6331-6344 (2018).

18. Kato, M. et al. Heterogeneous cancer-associated fibroblast population potentiates neuroendocrine differentiation and castrate resistance in a CD105-dependent manner. *Oncogene* **38**, 716-730 (2019).
19. Schoonderwoerd, M.J.A. et al. Targeting Endoglin Expressing Cells in the Tumor Microenvironment Does Not Inhibit Tumor Growth in a Pancreatic Cancer Mouse Model. *Onco Targets Ther* **14**, 5205-5220 (2021).
20. Hutton, C. et al. Single-cell analysis defines a pancreatic fibroblast lineage that supports anti-tumor immunity. *Cancer Cell* **39**, 1227-1244.e1220 (2021).
21. Fonsatti, E., Nicolay, H.J., Altomonte, M., Covre, A. & Maio, M. Targeting cancer vasculature via endoglin/CD105: a novel antibody-based diagnostic and therapeutic strategy in solid tumours. *Cardiovasc Res* **86**, 12-19 (2010).
22. Liu, Y., Paauwe, M., Nixon, A.B. & Hawinkels, L. Endoglin Targeting: Lessons Learned and Questions That Remain. *Int J Mol Sci* **22**, 147 (2020).
23. Dorff, T.B. et al. Bevacizumab alone or in combination with TRC105 for patients with refractory metastatic renal cell cancer. *Cancer* **123**, 4566-4573 (2017).
24. Mehta, C.R., Liu, L. & Theuer, C. An adaptive population enrichment phase III trial of TRC105 and pazopanib versus pazopanib alone in patients with advanced angiosarcoma (TAPPAS trial). *Ann Oncol* **30**, 103-108 (2019).
25. Choueiri, T.K. et al. 912PD - Results of the phase II TRAXAR study: A randomized phase II trial of axitinib and TRC105 (TRAX) versus axitinib (AX) alone in patients with advanced or metastatic renal cell carcinoma (mRCC). *Annals of Oncology* **30**, v362-v363 (2019).
26. Hamieh, M. et al. CAR T cell trogocytosis and cooperative killing regulate tumour antigen escape. *Nature* **568**, 112-116 (2019).
27. Greenman, R. et al. Shaping Functional Avidity of CAR T Cells: Affinity, Avidity, and Antigen Density That Regulate Response. *Mol Cancer Ther* **20**, 872-884 (2021).
28. Chung, J.Y. et al. Rapid CAR screening and circRNA-driven CAR-NK cells for persistent shed-resistant immunotherapy. *Signal Transduct Target Ther* **11**, 129 (2026).
29. Mansilla-Soto, J. et al. HLA-independent T cell receptors for targeting tumors with low

antigen density. *Nat Med* **28**, 345-352 (2022).
30. Werba, G. et al. Single-cell RNA sequencing reveals the effects of chemotherapy on human pancreatic adenocarcinoma and its tumor microenvironment. *Nature Communications* **14**, 797 (2023).
31. Davenport, A.J. et al. CAR-T Cells Inflict Sequential Killing of Multiple Tumor Target Cells. *Cancer Immunol Res* **3**, 483-494 (2015).
32. Xie, S. et al. Improved CAR internalization and recycling through transmembrane domain optimization reduces CAR-T cytokine release and exhaustion. *Frontiers in Immunology* **16**, 1531344 (2025).
33. Eyquem, J. et al. Targeting a CAR to the TRAC locus with CRISPR/Cas9 enhances tumour rejection. *Nature* **543**, 113-117 (2017).
34. Feucht, J. et al. Calibration of CAR activation potential directs alternative T cell fates and therapeutic potency. *Nature Medicine* **25**, 82-88 (2019).
35. Barisa, M. et al. Functional avidity of anti-B7H3 CAR-T constructs predicts antigen density thresholds for triggering effector function. *Nat Commun* **16**, 7196 (2025).
36. He, C. et al. CD19 CAR antigen engagement mechanisms and affinity tuning. *Sci Immunol* **8**, eadf1426 (2023).
37. Majzner, R.G. et al. Tuning the Antigen Density Requirement for CAR T-cell Activity. *Cancer Discov* **10**, 702-723 (2020).
38. Nam, G. et al. CD99-mediated immunological synapse formation potentiates CAR-T cell function. *Nature Communications* **16**, 7987 (2025).
39. Gad, A.Z. et al. Molecular dynamics at immune synapse lipid rafts influence the cytolytic behavior of CAR T cells. *Science Advances* **11**, eadq8114 (2025).
40. Wolf, F.A., Angerer, P. & Theis, F.J. SCANPY: large-scale single-cell gene expression data analysis. *Genome Biol* **19**, 15 (2018).
41. Korsunsky, I. et al. Fast, sensitive and accurate integration of single-cell data with Harmony. *Nat Methods* **16**, 1289-1296 (2019).
42. Bae, S. et al. CellDART: cell type inference by domain adaptation of single-cell and spatial transcriptomic data. *Nucleic Acids Res* **50**, e57 (2022).
43. Bae, S. et al. STopover captures spatial colocalization and interaction in the tumor microenvironment using topological analysis in spatial transcriptomics data. *Genome*

Medicine **17**, 33 (2025).
44. Schubert, M. et al. Perturbation-response genes reveal signaling footprints in cancer gene expression. *Nature Communications* **9**, 20 (2018).
45. Pham, D. et al. Robust mapping of spatiotemporal trajectories and cell-cell interactions in healthy and diseased tissues. *Nat Commun* **14**, 7739 (2023).
46. Davidson-Pilon, C. lifelines: survival analysis in Python. *Journal of Open Source Software* **4**, 1317 (2019).

Acknowledgements

We thank the Korea Basic Science Institute (Metropolitan Seoul Center) for access to the 3D holotomography system (CC008) and the confocal microscopy facility (SC242). We thank Professor Yong-Sung Kim (Ajou University) for providing the *S. cerevisiae* JAR200 and YVH10 strains. We thank the patients who donated tissue for this study.

Author contributions

M.J., C.H.L. and S.C.K. conceived and designed the study. S.H.S., J.S.H., D.E.K., S.M.Y., H.B.J., S.H.K., J.H.Y., H.W.L., J.J.H., Y.J.J., H.J.K., S.W.Y. and D.C.P. performed the experiments and data analysis. S.H.S. and J.S.H. wrote the original draft of the manuscript. M.J., C.H.L. and S.C.K. revised the manuscript, supervised the project and validated the final version. All authors read and approved the final manuscript.

Funding

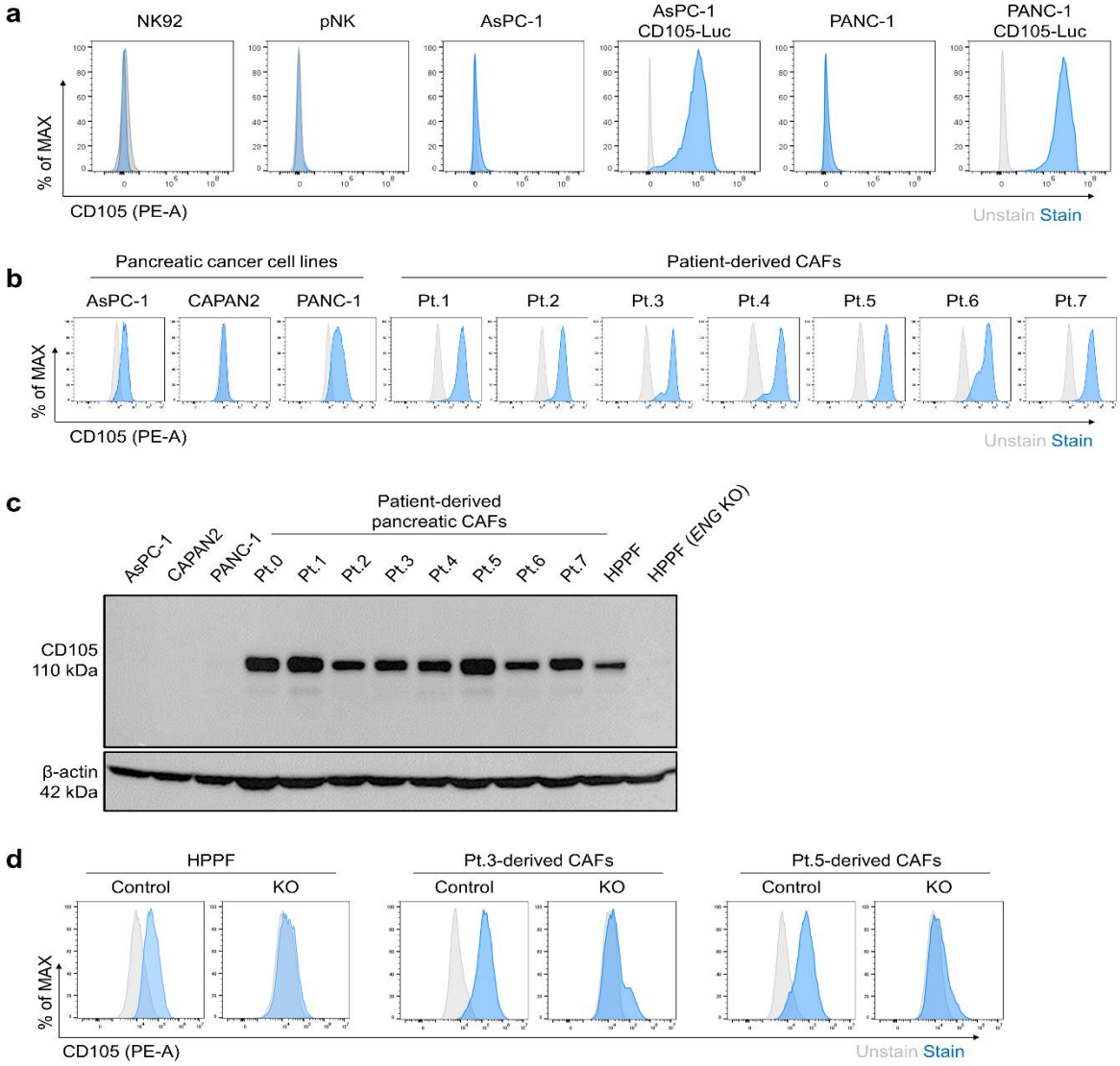
This work was supported by the National Research Foundation of Korea (NRF), funded by the Korean government (RS-2025-02216943 and RS-2026-25469890 to M.J.; RS-2023-00278980 and RS-2026-25527526 to C.H.L.). Additional funding was provided by the Korean Fund for Regenerative Medicine (KFRM), funded by the Korean government through the Ministry of

Science and ICT and the Ministry of Health and Welfare (RS-2026-25502076 to M.J.), and by the Korea Drug Development Fund (KDDF), funded by the Ministry of Science and ICT, the Ministry of Trade, Industry and Energy, and the Ministry of Health and Welfare (RS-2022-00166088 to M.J.). This work was also supported by the Korea Basic Science Institute under the R&D programme supervised by the Ministry of Science and ICT (S610000 and C612550). Further support was provided by a joint grant from the University of Ulsan and the Ulsan National Institute of Science and Technology, funded by the Ministry of Education (2025-0627 to S.C.K.), and by the Bio & Medical Technology Development Program of the NRF, funded by the Ministry of Science and ICT (RS-2025-16067734 to S.C.K.).

Competing interests

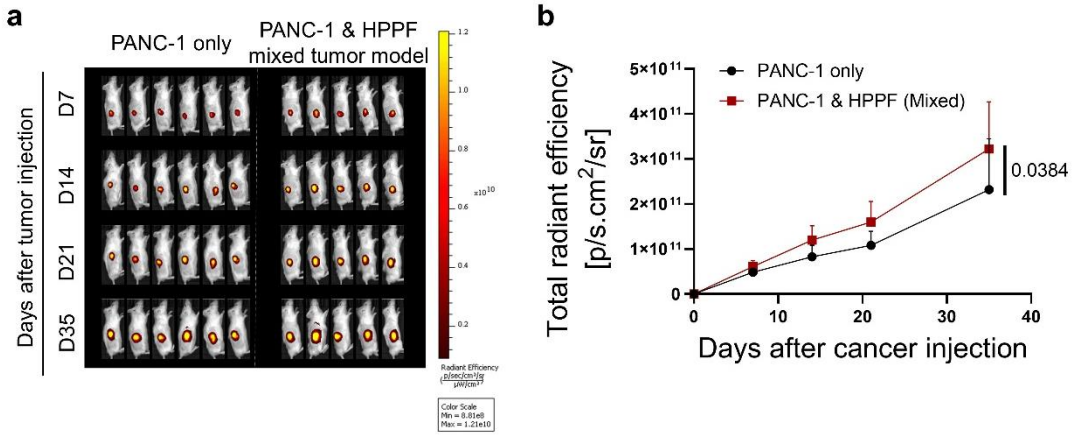
S.H.S., J.H.Y., J.S.H., C.H.L. and M.J. are listed as inventors on a patent application (KR 10-2023-0064534). The other authors declare no competing interests.

Correspondence and requests for materials should be addressed to Song Cheol Kim, Chang-Han Lee or Mihue Jang.

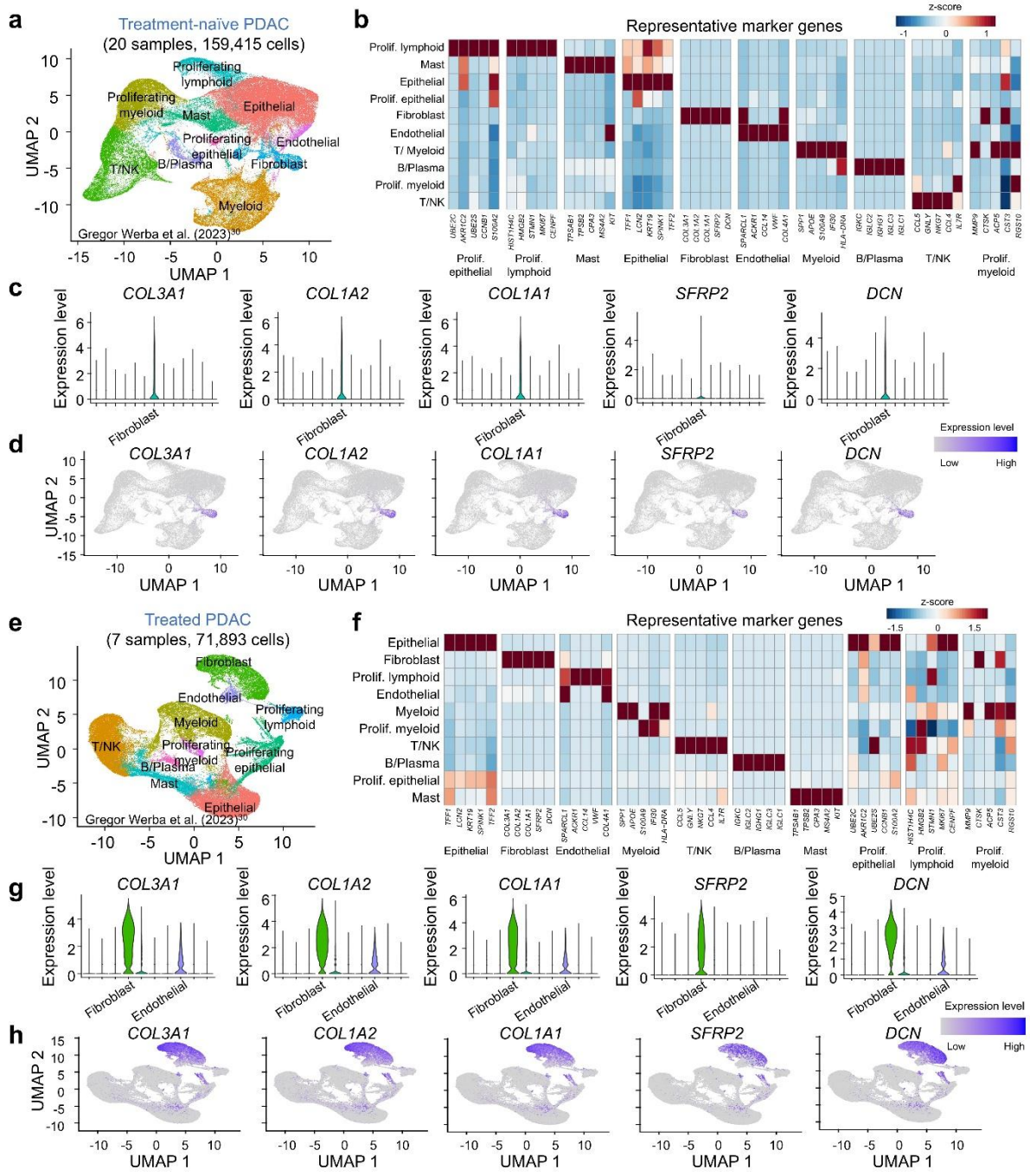


Extended Data Fig. 1. ENG/CD105 expression across pancreatic cancer and stromal cell types, and validation of *ENG* knockout (KO). a, Flow cytometry of surface ENG/CD105 in NK-92 cells, primary NK (pNK) cells, parental pancreatic cancer cell lines and CD105-overexpressing pancreatic cancer cells (AsPC-1-CD105-Luc and PANC-1-CD105-Luc). Grey histograms, unstained controls; blue histograms, ENG/CD105 staining. **b,** Flow cytometry of surface ENG/CD105 in pancreatic cancer cell lines and patient-derived CAFs. Grey histograms, unstained controls; blue histograms, ENG/CD105 staining. **c,** Immunoblot of ENG/CD105 in

pancreatic cancer cell lines, patient-derived CAFs, HPPFs and *ENG*-KO HPPFs. β-actin was the loading control. **d,** Flow-cytometric validation of ENG/CD105 expression in HPPFs and patient-derived CAFs after CRISPR–Cas9 ribonucleoprotein-mediated *ENG* KO. Grey histograms, unstained controls; blue histograms, CD105 staining.

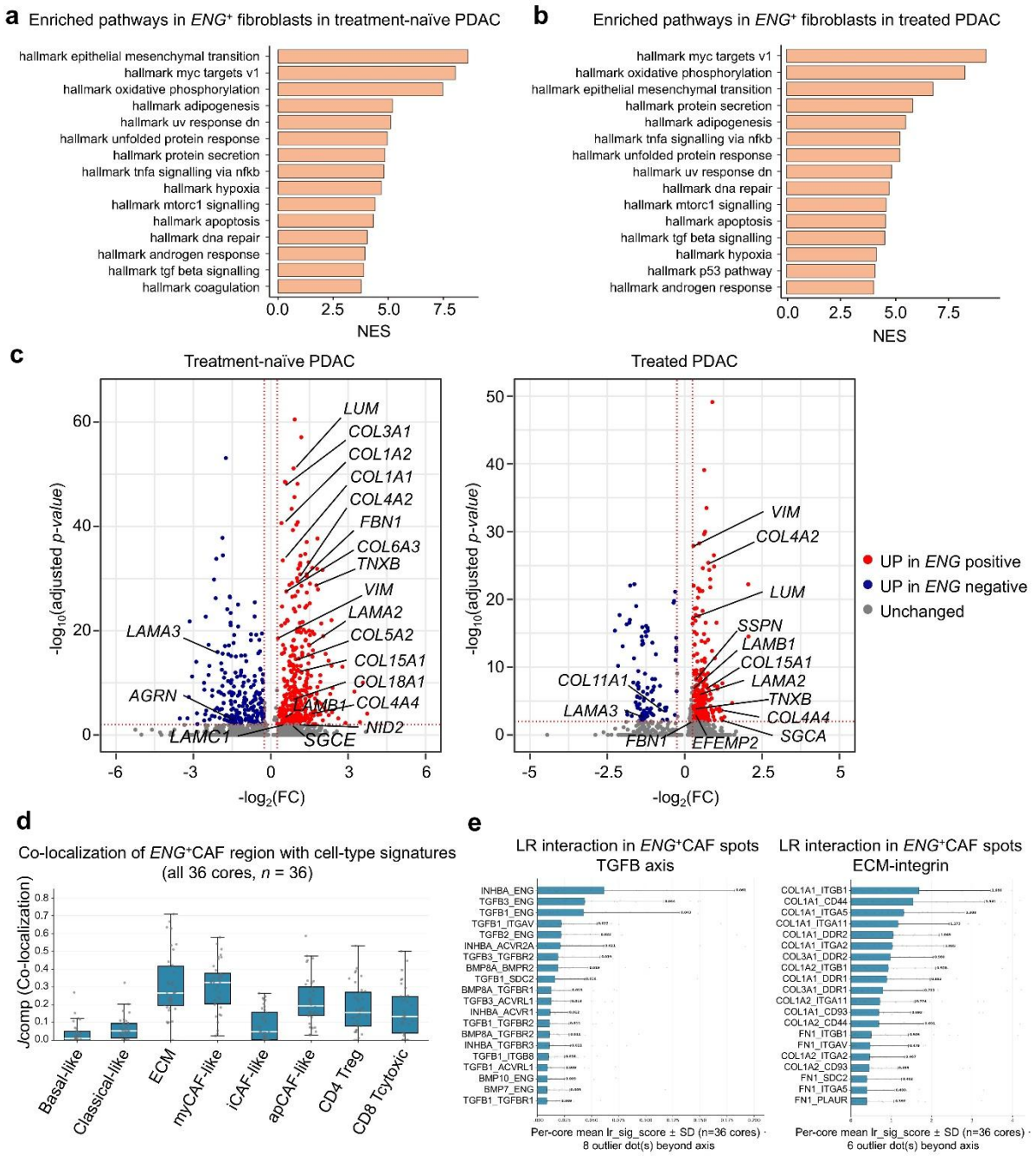


Extended Data Fig. 2. Pancreatic fibroblasts enhance PANC-1 tumour growth *in vivo*. a, Representative longitudinal fluorescence images of mice bearing PANC-1-mCherry tumours implanted alone or co-implanted with HPPFs, acquired on the indicated days after tumour injection. **b,** Quantification of total radiant efficiency in PANC-1-only and PANC-1/HPPF mixed-tumour xenografts over time ($n = 6$ mice for PANC-1 only and 5 for mixed group). Data are mean ± s.d. *P* value was determined using two-way ANOVA followed by Šídák's multiple comparisons test.



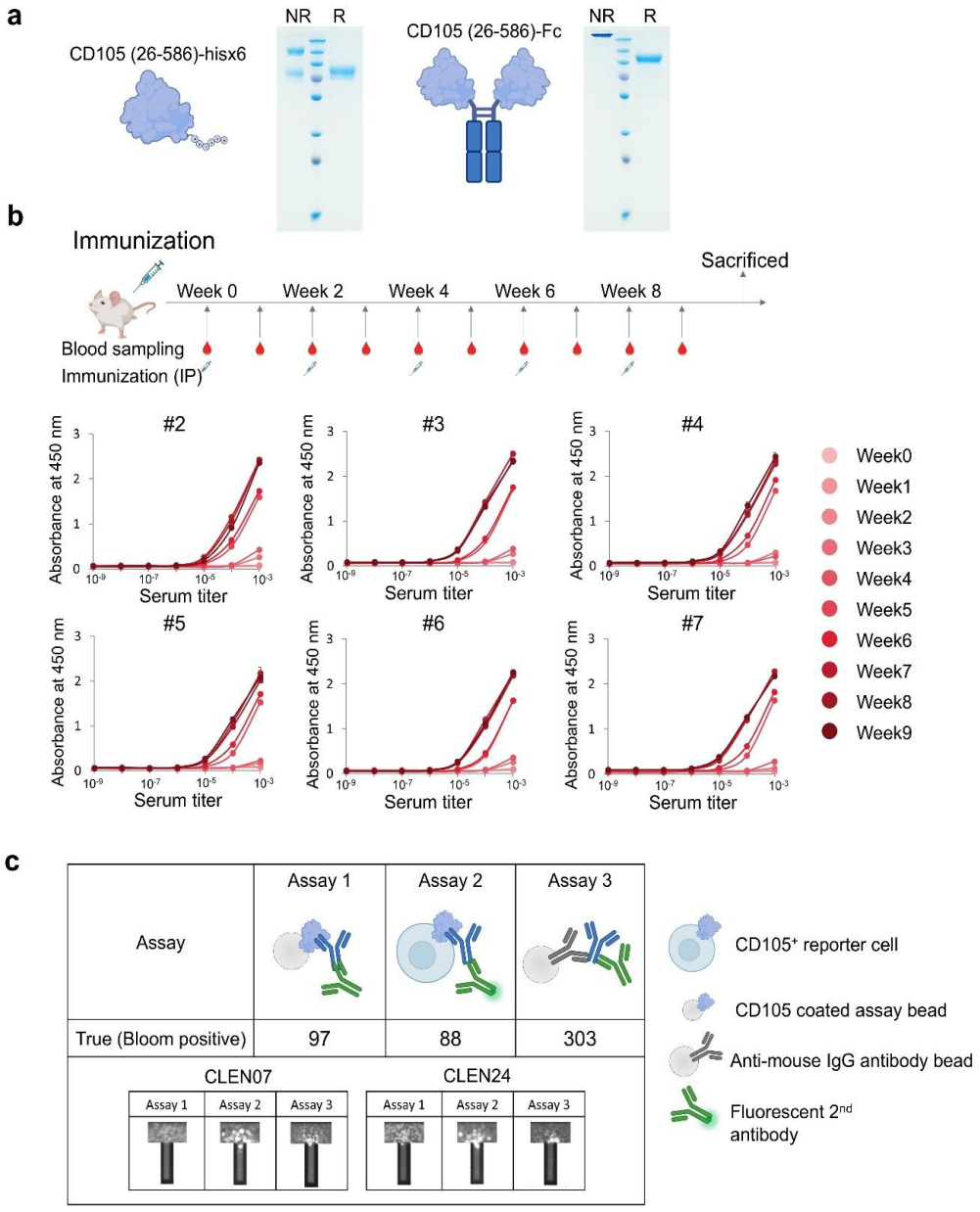
Extended Data Fig. 3. Annotation and validation of fibroblast populations in human PDAC single-cell RNA-sequencing datasets. a, UMAP of treatment-naïve PDAC single-cell RNA-sequencing data showing annotated major cell compartments. **b,** Heatmap of representative marker-gene expression across annotated populations in treatment-naïve PDAC tumours. **c,d,** Violin plots and UMAP feature plots showing expression of canonical fibroblast

markers (*COL3A1*, *COL1A2*, *COL1A1*, *SFRP2* and *DCN*) in treatment-naïve PDAC tumours. **e,** UMAP of treated PDAC single-cell RNA-sequencing data showing annotated major cell compartments. **f,** Heatmap of representative marker-gene expression across annotated populations in treated PDAC tumours. **g,h,** Violin plots and UMAP feature plots showing expression of canonical fibroblast markers in treated PDAC tumours.



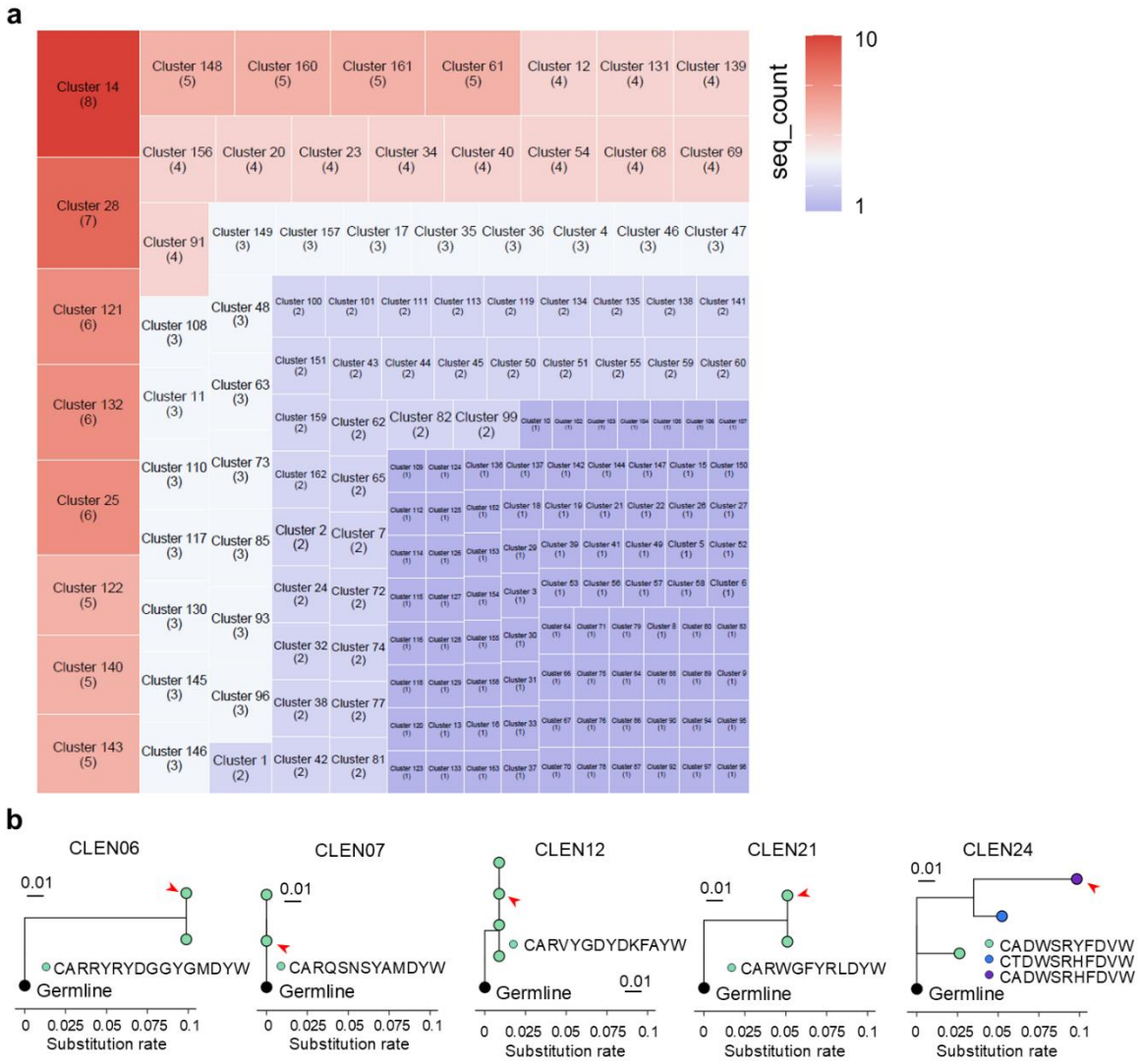
Extended Data Fig. 4. *ENG*⁺ fibroblasts are enriched for TGF-β- and ECM-remodelling programmes and occupy matrix-rich stromal niches in PDAC. a,b, Hallmark gene set enrichment analysis showing pathways enriched in *ENG*⁺ compared with *ENG*⁻ fibroblasts from treatment-naïve (**a**) and treated (**b**) PDAC samples. Bars indicate normalized enrichment

scores (NES). **c,** Volcano plots showing differentially expressed genes between *ENG*$^{+}$ and *ENG*$^{-}$ fibroblasts from treatment-naïve and treated PDAC samples. Selected ECM- and fibroblast-associated genes are labelled; significance thresholds are indicated by the red dashed lines. **d,** Spatial transcriptomic analysis of *ENG*$^{+}$ CAF regions showing co-localization with tumour, stromal and immune cell-state signatures across PDAC spatial transcriptomic cores. Co-localization was quantified using the composite Jaccard index (J_{comp}). Box plots show the median, interquartile range and whiskers; individual points represent tumour cores (n = 36 cores). **e,** Ligand–receptor interaction analysis in *ENG*$^{+}$ CAF-enriched spots showing the top-ranked interactions in the TGF-β axis (left) and the ECM–integrin signalling axis (right). Bars represent per-core mean ligand–receptor signalling scores ± s.d. across 36 tumour cores.

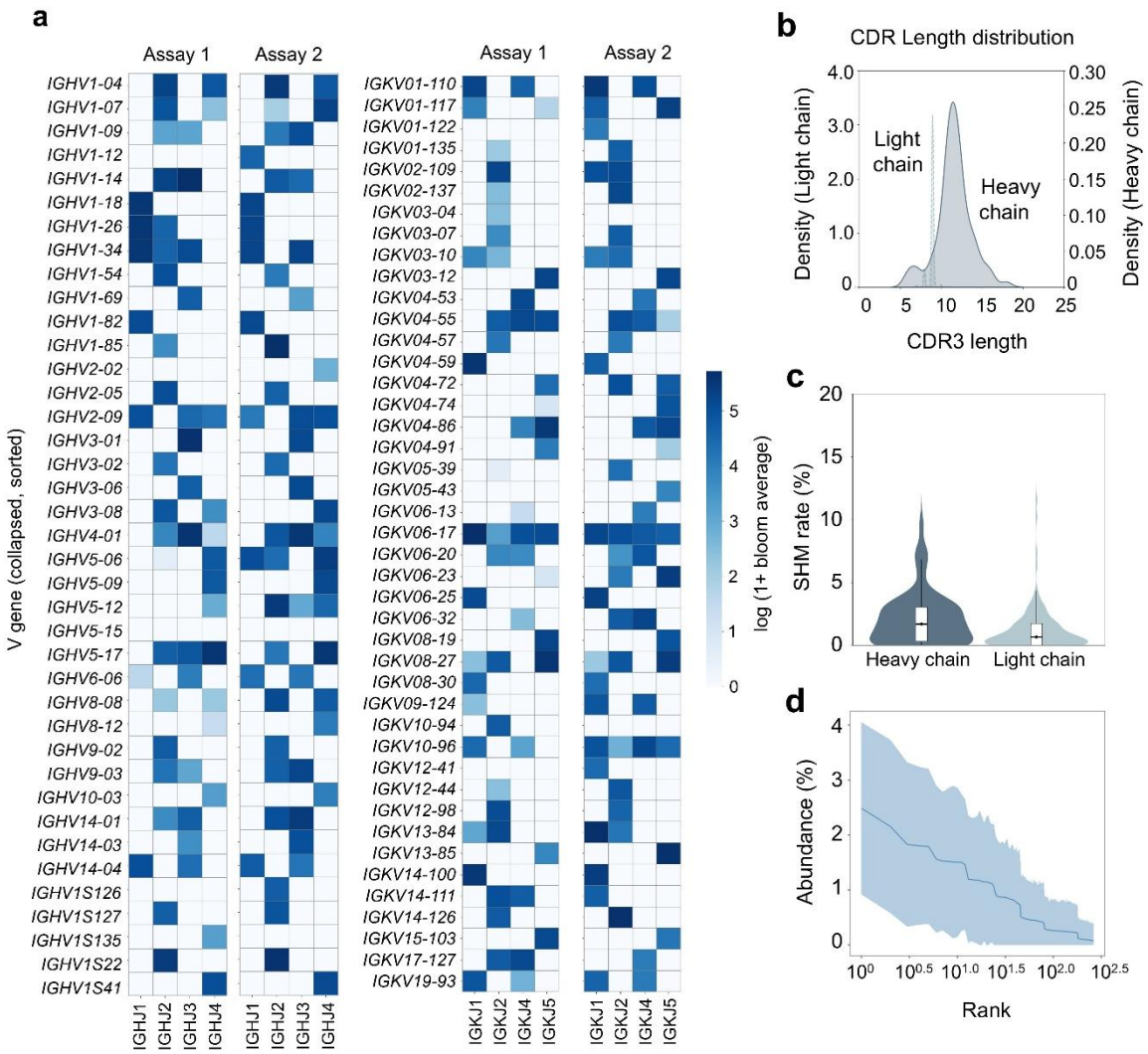


Extended Data Fig. 5. Recombinant CD105 antigen preparation and plasma B-cell screening workflow. a, Recombinant CD105 antigens used for mouse immunization and screening. Purified CD105(26–586)-His_6 and CD105(26–586)-Fc proteins were analysed under non-reducing (NR) and reducing (R) conditions. **b**, Immunization schedule and serum

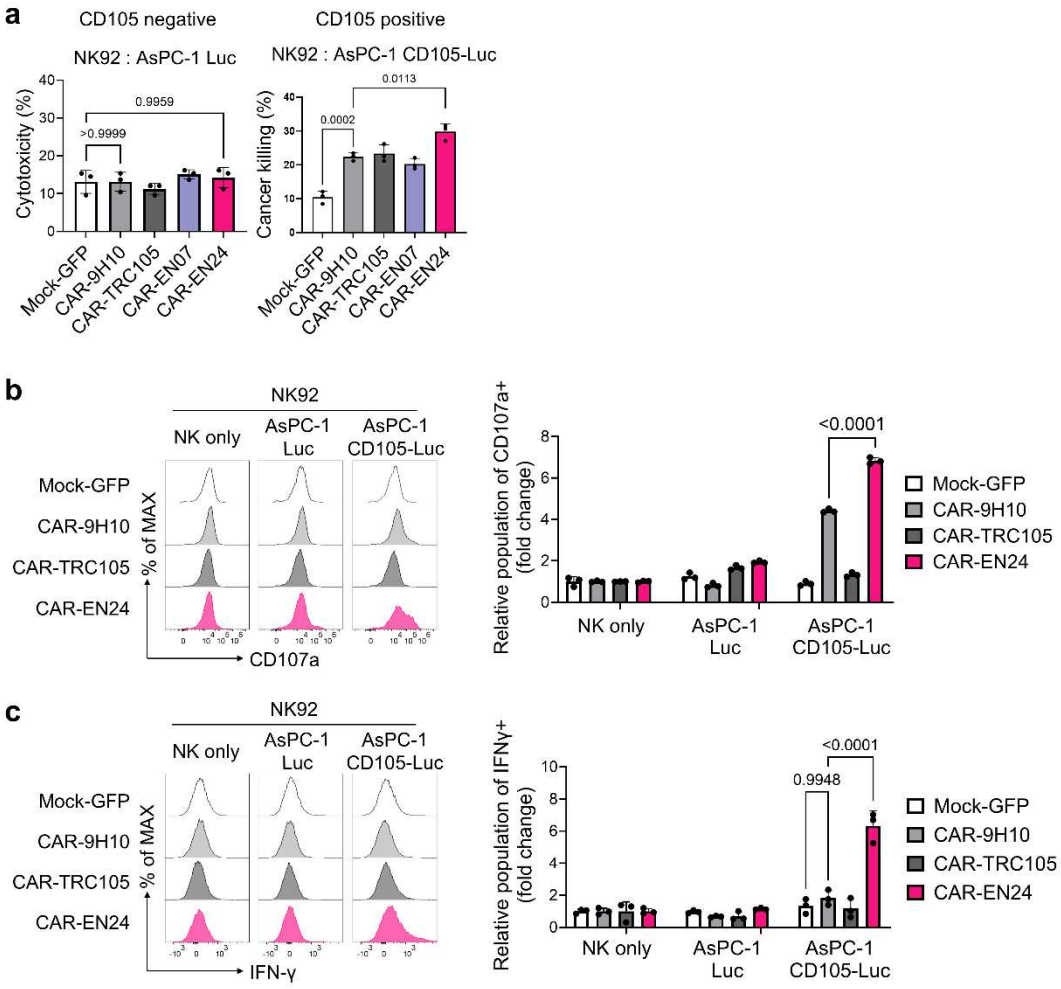
antibody responses in CD105-immunized mice. Serum reactivity against recombinant CD105 was measured by ELISA at the indicated time points (n = 6 mice). Each serum sample was analysed in duplicate. **c,** Summary of Beacon optofluidic screening assays used to identify CD105-reactive plasma cells. $CD138^{+}$ plasma cells were screened for recombinant CD105 binding, $CD105^{+}$ reporter cell binding and IgG secretion. Representative positive events for CLEN07 and CLEN24 are shown.



Extended Data Fig. 6. Clonal clustering of CD105-reactive antibody sequences recovered from plasma B-cell screening. a, Treemap showing clonal clusters of antibody sequences recovered from CD105-reactive plasma-cell events identified by Beacon screening. Each rectangle represents a clonal cluster and the number in parentheses indicates the sequence count within that cluster. Colour intensity denotes sequence abundance, with red indicating higher and blue lower sequence counts. **b,** Phylogenetic trees of selected CD105-reactive antibody clones showing sequence relationships to inferred germline sequences. Branch length represents substitution rate. IGH CDR3 amino acid sequences are indicated for each representative clone; red arrowheads mark the sequences selected for subsequent characterization, one per clonal cluster.



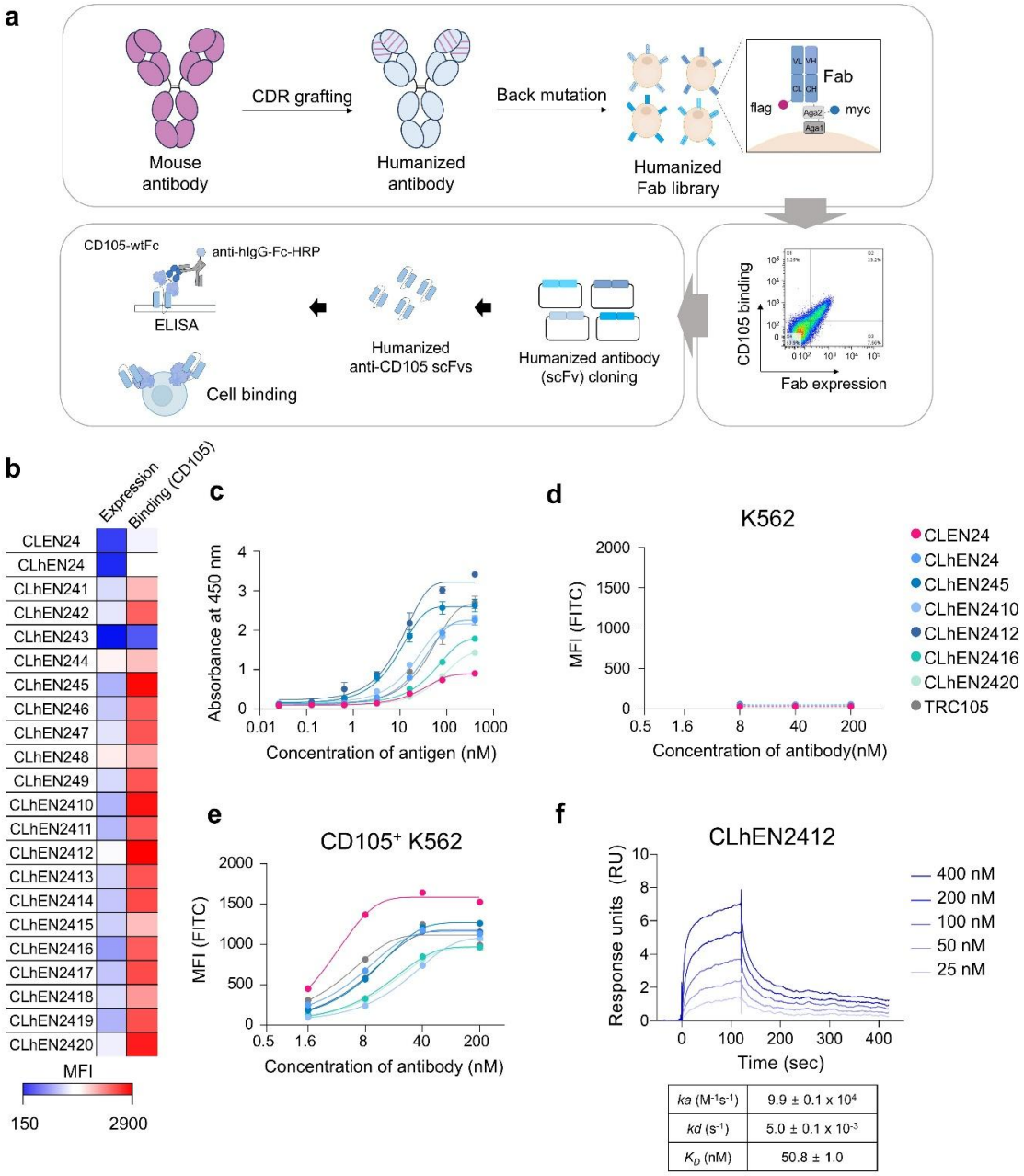
Extended Data Fig. 7. Repertoire-level characterization of CD105-reactive antibody sequences recovered by plasma B-cell screening. a, Heatmap of immunoglobulin heavy-chain V/J gene usage among CD105-reactive antibody sequences recovered from Beacon assays 1 and 2. Colour intensity indicates log-transformed clonal abundance. **b,** CDR3 length distribution of recovered heavy- and light-chain sequences. **c,** Somatic hypermutation rates of heavy- and light-chain sequences. **d,** Rank-abundance plot showing clonal expansion patterns among recovered antibody sequences.



1486

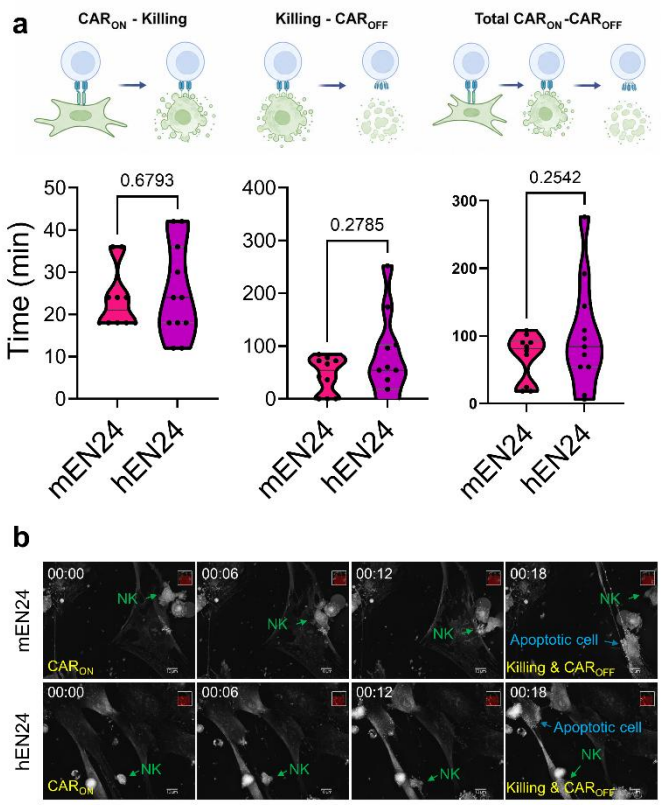
1487 **Extended Data Fig. 8. Antigen-dependent cytotoxicity and activation of CD105-targeted**
1488 **CAR-NK-92 cells. a,** Cytotoxicity of NK-92 cells expressing the indicated CD105-targeted
1489 CARs against CD105-negative AsPC-1-Luc and CD105-positive AsPC-1-CD105-Luc cells (*n*
1490 = 3). **b,** Representative flow cytometry histograms and quantification of CD107a expression in
1491 CAR-NK-92 cells cultured alone or co-cultured with AsPC-1-Luc or AsPC-1-CD105-Luc
1492 target cells (*n* = 3). **c,** Representative flow cytometry histograms and quantification of IFN-γ
1493 expression in CAR-NK-92 cells cultured alone or co-cultured with the same target cells (*n* =
1494 3). Data are mean ± s.d. unless otherwise indicated. Statistical significance was determined

using one-way ANOVA with Tukey's multiple comparisons.



Extended Data Fig. 9. Humanization and binding validation of the CLEN24 anti-CD105 antibody. a, Schematic of the CLEN24 humanization workflow. Parental CLEN24 was

humanized by CDR grafting and framework back-mutation, followed by screening of a humanized Fab library, scFv cloning and validation by ELISA and cell-surface binding assays. The CDR-grafted precursor was designated CLhEN24, and the lead humanized clone CLhEN24-12 is designated hEN24 when expressed as a CAR. **b,** Heatmap summarizing expression and CD105-binding activity of humanized CLEN24 variants. **c,** ELISA binding of selected humanized CLEN24 variants to recombinant CD105-wtFc (n = 3 independent experiments). **d,e,** Flow cytometric analysis of selected humanized CLEN24 variants binding to parental K562 cells (**d**) and $CD105^+$ K562 cells (**e**), shown as FITC mean fluorescence intensity (n = 3 independent experiments). TRC105 and parental CLEN24 were included as reference antibodies. **f,** Representative SPR sensorgrams and SPR-derived kinetic parameters for the CLhEN24-12 scFv binding to recombinant CD105 (n = 3 independent experiments). Association rate constant (k_{on}), dissociation rate constant (k_{off}) and equilibrium dissociation constant (K_D) are shown. Data are mean ± s.d.



Extended Data Fig. 10. Humanized EN24-derived CARs retain anti-CD105 activity in primary NK cells. Quantification (**a**) and representative time-lapse images (**b**) of CAR on/off dynamics in mouse EN24 (mEN24)- and humanized EN24 (hEN24)-CAR-pNK cells during engagement with CD105^{+} target cells (n = 10 for mEN24 and 11 for hEN24 effector–target conjugates per construct). Scale bars, 10 μm. Data are mean ± s.d. Statistical significance was determined using unpaired two-tailed t-tests.

Supplementary Files

This is a list of supplementary files associated with this preprint. Click to download.

- SupplementaryVideo4Pt.5ENGKO.mp4
- SupplementaryVideo8MockNK.mp4
- SupplementaryVideo6CAREN24.mp4
- SupplementaryVideo5CAR9H10.mp4
- SupplementaryVideo10Nontreatment.mp4
- SupplementaryVideo14Sequentialcombi.mp4
- SupplementaryVideo7nontreatment.mp4
- SupplementaryVideo2Pt.3ENGKO.mp4
- NatBMESupplementaryfinal2601005.docx
- SupplementaryVideo9CAREN24.mp4
- SupplementaryVideo12CAR9H10.mp4
- SupplementaryVideo11MSLNCARNK.mp4
- SupplementaryVideo1Pt.3sgControl.mp4
- SupplementaryVideo3Pt.5sgControl.mp4
- SupplementaryVideo13CARhEN24.mp4